SANDIA REPORT
SAND2019-12275
Printed September 2019

Sandia National Laboratories

Shortening the Design and Certification Cycle for Additively Manufactured Materials by Improved Mesoscale Simulations and Validation Experiments: Fiscal Year 2019 Status Report

Paul Specht, John Mitchell, David Adams, Justin Brown, Stewart Silling, and Jack Wise
Sandia National Laboratories

Todd A. Palmer
Pennsylvania State University

Prepared by
Sandia National Laboratories
Albuquerque, New Mexico
87185 and Livermore,
California 94550

Issued by Sandia National Laboratories, operated for the United States Department of Energy by National Technology & Engineering Solutions of Sandia, LLC.

Available to DOE and DOE contractors from
U.S. Department of Energy
Office of Scientific and Technical Information
P.O. Box 62
Oak Ridge, TN 37831

Telephone: (865) 576-8401
Facsimile: (865) 576-5728
E-Mail: reports@osti.gov
Online ordering: http://www.osti.gov/scitech

Available to the public from
U.S. Department of Commerce
National Technical Information Service
5301 Shawnee Rd
Alexandria, VA 22312

Telephone: (800) 553-6847
Facsimile: (703) 605-6900
E-Mail: orders@ntis.gov
Online order: https://classic.ntis.gov/help/order-methods/

ABSTRACT

This report outlines the fiscal year (FY) 2019 status of an ongoing multi-year effort to develop a general, microstructurally-aware, continuum-level model for representing the dynamic response of material with complex microstructures. This work has focused on accurately representing the response of both conventionally wrought processed and additively manufactured (AM) 304L stainless steel (SS) as a test case. Additive manufacturing, or 3D printing, is an emerging technology capable of enabling shortened design and certification cycles for stockpile components through rapid prototyping. However, there is not an understanding of how the complex and unique microstructures of AM materials affect their mechanical response at high strain rates. To achieve our project goal, an upscaling technique was developed to bridge the gap between the microstructural and continuum scales to represent AM microstructures on a Finite Element (FE) mesh. This process involves the simulations of the additive process using the Sandia developed kinetic Monte Carlo (KMC) code SPPARKS. These SPPARKS microstructures are characterized using clustering algorithms from machine learning and used to populate the quadrature points of a FE mesh. Additionally, a spall kinetic model (SKM) was developed to more accurately represent the dynamic failure of AM materials. Validation experiments were performed using both pulsed power machines and projectile launchers. These experiments have provided equation of state (EOS) and flow strength measurements of both wrought and AM 304L SS to above Mbar pressures. In some experiments, multi-point interferometry was used to quantify the variation is observed material response of the AM 304L SS. Analysis of these experiments is ongoing, but preliminary comparisons of our upscaling technique and SKM to experimental data were performed as a validation exercise. Moving forward, this project will advance and further validate our computational framework, using advanced theory and additional high-fidelity experiments.

ACKNOWLEDGEMENTS

The authors greatly appreciate the support of Mike Saavedra in machining the experimental samples. The authors would also like to thank the Dynamic Integrated Compression facility (DICE) staff for executing the Thor experiments: Brian Stoltzfus, Randy Hickman, Keith Hodge, Joshua Usher, Lena Pacheco, and Eric Breden. The authors would also like to thank the staff at the Shock Thermodynamics Applied Research (STAR) facility for executing the plate impact experiments: Scott Alexander, Bill Reinhart, Bernardo Farfan, Rocky Palomino, John Martinez, and Rafael Sanchez. Lastly, the authors would like to acknowledge the development support of Jason Sanchez in ALEGRA to incorporate our upscaling method and Michael Powell for helping with post processing scripts for results analysis.

CONTENTS

LIST OF FIGURES

LIST OF TABLES

This page left blank

ACRONYMS AND DEFINITIONS

Abbreviation	Definition
AB	Sample A/Sample B
AK	Anode-Cathode
ALE	Arbitrary Lagrangian Eulerian
AM	Additive Manufacturing
CW	Continuous Wave
DED	Direct Energy Deposition
DICE	Dynamic Integrated Compression Experimental
EBSD	Electron Backscatter Diffraction
EDM	Electro-Discharge Machining
EOS	Equation of State
FE	Finite Element
FY	Fiscal Year
ILA	Inverse Lagrangian Analysis
IO	Input/Output
JC	Johnson-Cook
KMC	Kinetic Monte Carlo
LENS™	Laser Engineered Net Shaping
MHD	Magnetohydrodynamic
PCI	Phase Contrast Imaging
PDV	Photonic Doppler Velocimetry
PMMA	Polymethylmethacrylate
PSP	Process-Structure-Property
PSU	Pennsylvania State University
RMI	Richtmyer-Meshkov Instability
SEM	Scanning Electron Microscopy
SG	Steinberg-Guinan
SKM	Spall Kinetic Model
SPPARKS	Stochastic Parallel PARticle Kinetic Simulator
SS	Stainless Steel
STAR	Shock Thermodynamics Applied Research
VISAR	Velocity Interferometer System for Any Reflector
VPF	Velocity Per Fringe

1. INTRODUCTION AND PROJECT OBJECTIVES

Additive manufacturing (AM), or 3D printing, describes a variety of manufacturing techniques in which material is deposited layer-by-layer in an additive fashion to achieve a final form [1, 2, 3, 4, 5, 6, 7]. This contrasts with traditional machining methods that rely on subtractive methods to produce the desired shape. The rapid prototyping and complex topologies achievable with AM have potential to provide lower cost, higher performing parts for the stockpile. However, the variability that plagues the AM process presents a major hurdle to certification. For these reasons, understanding how the AM fabrication process alters the AM material microstructure and influences the observed material response, termed Process-Structure-Property (PSP) relationships, is an area of emphasis in the National Nuclear Security Administration [8].

This work investigates the PSP relationship in a single material: 304L stainless steel (SS). The response of AM 304L SS is compared to that of a conventionally wrought processed 304L SS. The AM 304L SS in this study was made with laser engineered net shaping (LENS^{TM}) [9, 10], which is a directed energy deposition (DED) method [7]. The decision to focus on 304L SS was made for two reasons: it is a common engineering alloy in the stockpile and a prior study investigated the mechanical response of wrought and LENS^{TM} 304L SS over a wide range of strain rates [11]. This work utilized an AM 304L SS made with the same processing conditions and on the same machine as that prior study [11] to augment that data set by:

- Developing a computationally tractable method for incorporating complex microstructural information into simulations.
- Focusing on the high pressure, high strain rate ($> 10^5$ s^{-1}) response.

The complex microstructures generated by the rapid cooling rates in the LENS^{TM} process are believed to influence the observed response at high strain rates.

The goal of this work is to identify a computational framework, verified by high-fidelity experiments, that can shorten the design and certification cycle of AM components. Due to the complex microstructures present in AM materials, a new model capability is needed to represent these materials with reasonable computational costs. The project employs direct integration of material characterization, computational prediction, and experimental validation to understand the observed material response. From this integrated approach, a general, microstructurally-aware computational method was developed to tractably represent material with complex microstructures, such as AM alloys. Such a framework can help in understanding of how the unique microstructures of AM material influence its observed response and, through sensitivity studies, reduce the design space of future AM components in the stockpile.

In this report, we detail the work accomplished to date on studying the high strain-rate response of AM 304L SS. In addition, we present our path forward to achieving a computational framework to shorten the design and certification cycle. Section 2 briefly describes the wrought and AM 304L SS materials studied. Section 3 describes the progress towards developing our computational framework. It discusses an upscaling technique for representing AM microstructures on continuum meshes in Section 3.1 and the development of a continuum-level spall kinetic model (SKM) in Section 3.2. Section 4 describes the validation experiments performed. They include pulsed power experiments on both Thor and Z in Section 4.1 and projectile impact experiments performed at the Shock Thermodynamics Applied Research (STAR) facility in Section 4.2. Section 5 describes our validation activities for both the upscaling (Section 5.1) and SKM (Section 5.2). Lastly, this report outlines the planned next for the project in Section 6.

2. DESCRIPTION OF SAMPLE MATERIAL

The wrought and AM 304L SS investigated in this work are described below. The AM 304L SS studied was made on the same machine with the same fabrication parameters as that previously investigated in referenced [11]. Individual surveys of AM 304L SS microstructure (grain structure, composition, phase, etc.) were completed on sample pieces extracted from each AM build obtained for this work to ensure uniform material characteristics with the prior material in reference [11]. In general, the material properties, phase, and microstructure of these materials are essentially identical to those of the prior material [11].

2.1. Characteristics of the Wrought 304L SS Used for Mechanical Testing

The wrought 304L SS was ingot derived, re-melted material provided originally by Honeywell Federal Manufacturing and Technology (Kansas City). It was attained as a controlled-sulfur, weld-critical composition (specified in Table 2-1). The wrought material is mostly austenite. Both Feritscope and X-ray diffraction show that there is ~1 – 3 % ferrite in the starting material. A separate, previous materials certification claimed the material to have between 0.6 and 1.2 % ferrite [11]. The microstructure of wrought material, characterized by large area electron backscatter diffraction (EBSD) maps, was composed of austenite grains of size ~10s of micrometers. An EBSD map of wrought 304L SS is included in Figure 2-1. Austenite grains are equiaxed. The ferrite appeared as elongated stringers with long axis aligned with the axis of the cylindrical billet. There continues to be no evidence of voids in the wrought baseline material (i.e., prior to mechanical tests).

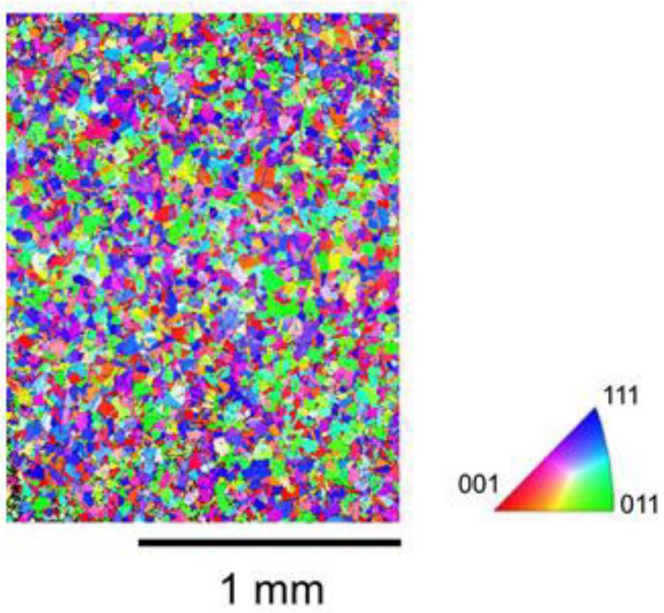

Figure 2-1. EBSD image of wrought 304L SS (Left). Each color corresponds to a different crystallographic orientation as indicated by the color map (Right).

Samples were extracted from wrought billets by electro-discharge machining (EDM). Samples were removed from the center volume of the provided billets for the majority of experiments. This helped ensure similar mechanical characteristics among wrought test samples thus avoiding a known, hardness variation with billet radius [11]. Sample blanks were removed by wire EDM and then

finished by lathe turning, milling or polishing to meet test requirements. Samples were typically made by aligning the mechanical load direction with the wrought cylinder axis. This convention matches prior studies [11]. Samples extracted from cylindrical wrought billets were tested in the as-finished metallurgical state.

Table 2-1. Elemental composition of the wrought 304L SS

Elemental Constituent	Composition (wt. %)	Elemental Constituent	Composition (wt. %)
C	0.013	Ni	10.1
Cr	19.5	O	n/m
Cu	n/m	P	0.015
Mn	1.5	S	0.015
Mo	0.027	Si	0.58
N	0.049	V	0.02

2.2. Characteristics of the AM 304L SS Used for Mechanical Testing

2.2.1. AM Fabrication Process

Square, AM 304L SS bars were fabricated using a custom, additive manufacturing system located at Pennsylvania State University (PSU). Continuous wave (CW) laser light was delivered from an IPG Photonics® YLR-12000-L ytterbium fiber laser, which has an operating wavelength ranging from 1070 to 1100 nm. The light was directed to the workpiece through a 600 μm diameter fiber into a copper-cooled reflective optics system. The collimator had a diameter of 49.5 mm and a focal length of 125 mm, while the focusing optics had the same diameter and a focal length of 600 mm. Reflective optics were utilized to avoid thermal lensing effects observed in the use of high-power transmissive optics in other systems. Powder was delivered to the build surface using a Powder Feed Dynamics Mark XV Precision Powder Feeder and a custom-designed four nozzle powder delivery system. The build chamber was purged with ultra-high purity Ar during DED. The chamber atmosphere was controlled by an MBraun Model MB 200G gas purifier, and the gaseous oxygen levels were measured using a General Electric CGA 351 zirconium oxide Oxygen Analyzer. Attempts to maintain oxygen levels below 110 ppm using this approach proved successful.

Stainless steel bars were built using Micro-melt powder (44 to 10 micrometers size) from Carpenter Powder Products. This powder was manufactured using a nitrogen-atomization processes. The supplier's certified composition is listed in Table 2-2. Some changes in composition were detected after building – attributed to volatilization during fabrication [11]. Mainly, there was a reduction in the Cr concentration by < 0.25 wt.%. Mn and Ni were also reduced by ~ 0.05 and 0.1 wt.%, respectively. The N content was potentially reduced by ~0.01 wt.%. All of these changes are taken with respect to starting powder composition.

An incident CW laser power of 3.8 kW was used to build square bars having approximate dimensions of 10 x 10 x 2.5 cm (example shown in Figure 2-2). The powder flow rate was set to 23 g/min for each build. The AM process utilized a parallel scan geometry, meaning the stage and base plate were translated in linear paths that were reproduced in subsequent layers. The table speed was

set at 63.5 cm/min. The hatch spacing, or separation between adjacent scan lines within a layer, was set to 1.925 mm. The build rate was determined to be 1.27 mm/layer. The AM process started by placing a substrate (a wrought 304L SS base plate) 10 mm from the gas nozzle exits as this corresponds to the focus point of the powder flow. At this location, the laser beam is deliberately defocused. The beam therefore has a measured diameter equal to 4 mm.

Table 2-2. Chemical composition of 304L SS powder used for additive manufacturing (as certified by Carpenter Powder Products)

Elemental Constituent	Composition (wt. %)	Elemental Constituent	Composition (wt. %)
C	0.013	S	0.008
Si	0.55	Cr	18.9
Mn	1.38	Ni	9.9
P	0.009	Fe	remainder

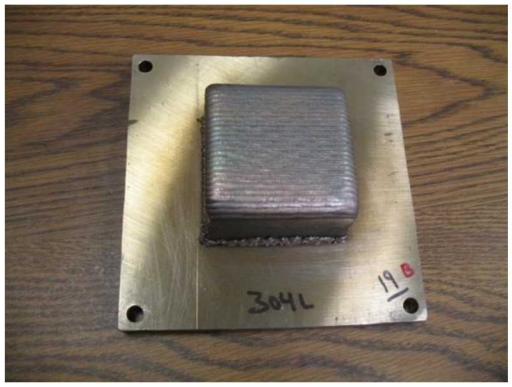

Figure 2-2. Photograph of AM 304L SS square bar on the wrought 304L SS base plate.

2.2.2. Directional Nomenclature of the AM 304L SS

The AM bars are described using a Cartesian notation that is largely consistent with the ASTM standard [12]. Three letters (X, Y and Z) reference the key directions associated with additive processing. Specifically, Z designates the net build direction, and is parallel with (but opposite to) the downward-directed laser vector. X and Y are the orthogonal in-plane stage scan directions. Both lie perpendicular to Z, thus forming a Cartesian coordinate system. The dominant scan line direction is designated as X, while the hatch direction is designated Y.

Knowing that the material was built up layer by layer using a scanned stage approach, one should expect different solidified microstructures when viewing different faces. Referencing Figure 2-3, the Z face shows the material from a top down perspective. Alternatively, one sees microstructural artifacts associated with individual scan lines through multiple layers when viewing a polished X face. The Y direction corresponds to the step over direction in adjacent lines (hatch). Thus, a polished X face potentially shows microstructural artifacts associated with this period. The Y face simply shows the through-thickness structure that is associated with overlaid laser scan lines but without evidence for hatch or beam width.

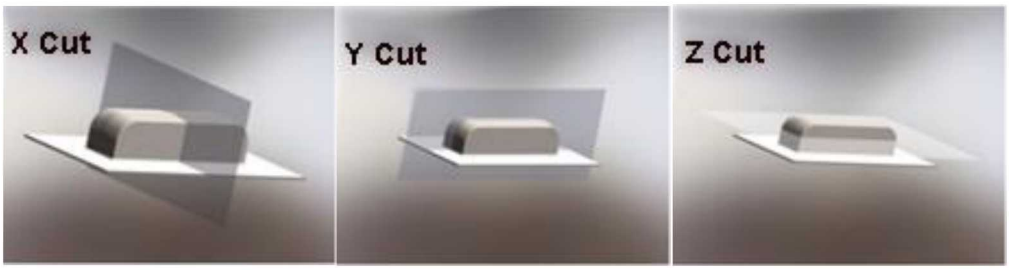

Figure 2-3. Depictions using a semi-transparent plane to portray the locations of X, Y, and Z planes of an additive block having a dominant scan direction (left-to-right). The build direction is taken to be Z. The block is shown attached to a thinner, wider base plate.

This letter nomenclature is also adopted when describing the material axis of loading for dynamic experiments. The square bars were most often formed into discs or thin large area samples by EDM for subsequent testing. All experimental samples reference a primary additive direction (X-Cut, Y-Cut, or Z-Cut) when describing the axis of loading which is the direction normal to the produced face.

2.2.3. Microstructural Characteristics of the AM 304L SS

Samples were prepared for microstructural characterization by cutting along different orientations of interest and polishing. Samples were first cut using an abrasive saw with water coolant or extracted by EDM. Extracted samples were then gently ground using SiC papers through 600 grit. Polishing started with a 9 μm slurry and was followed by 3 and then 1 μm slurries to remove all evidence of the grinding and provide a low deformation surface. Electropolishing prepared the final surface. This involved a Struers LetroPol 5 polisher with an electrolyte solution consisting of 600 mL methanol, 360 mL ethylene glycol mono-butyl ether and 60 mL perchloric acid (60%).

Microstructural analysis involved scanning electron microscopy (SEM) and EBSD imaging. The SEM utilized a Zeiss Supra 55VP field emission gun electron microscope and a K.E. Developments solid state backscattered electron detector. Channeling contrast was achieved by using an appropriate accelerating voltage and short working distance. EBSD utilized a Bruker detector and Esprit software.

The EBSD maps included in Figure 2-4 reveal large areas of the Z-Cut (Left) and X-Cut (Right) AM 304L SS. The map dimensions are ~6.5 x 7.5 mm in both cases. The Z-Cut AM 304L SS (Left side of Figure 2-4) shows evidence of the dominant laser scan direction which is up in the map. Also, one readily detects the ~ 2 mm hatch, which is a displacement between scan lines, oriented left to right. The X-Cut AM 304L SS (Right side of Figure 2-4), one views through several layers of deposited stainless steel. Again, the hatch is evident when viewing left to right.

The indexed Kikuchi diffraction patterns that are used to generate these EBSD maps demonstrate that the AM 304L SS was nearly all austenite – consistent with XRD and Feritscope. If one sees a color (not black), then it has been successfully indexed as austenite. Ferrite appears black in this and other EBSD maps. Also important to our study which sought to produce dense material, EBSD maps show no lack-of-fusion defects, large voids or other defects near layer interfaces. The two dark regions in the upper left map of the Z-Cut AM 304L SS (Right side of Figure 2-4) were determined to be contamination from sample sectioning.

It is apparent from the EBSD maps and complimentary SEM images that grains orient epitaxially from one layer to the next. Inverse pole figures associated with this image show evidence for

preferred crystalline (100) texture in the X direction with (022) oriented in Y. AM stainless steel 304L grains are large, up to 1 mm or perhaps even larger in some volumes.

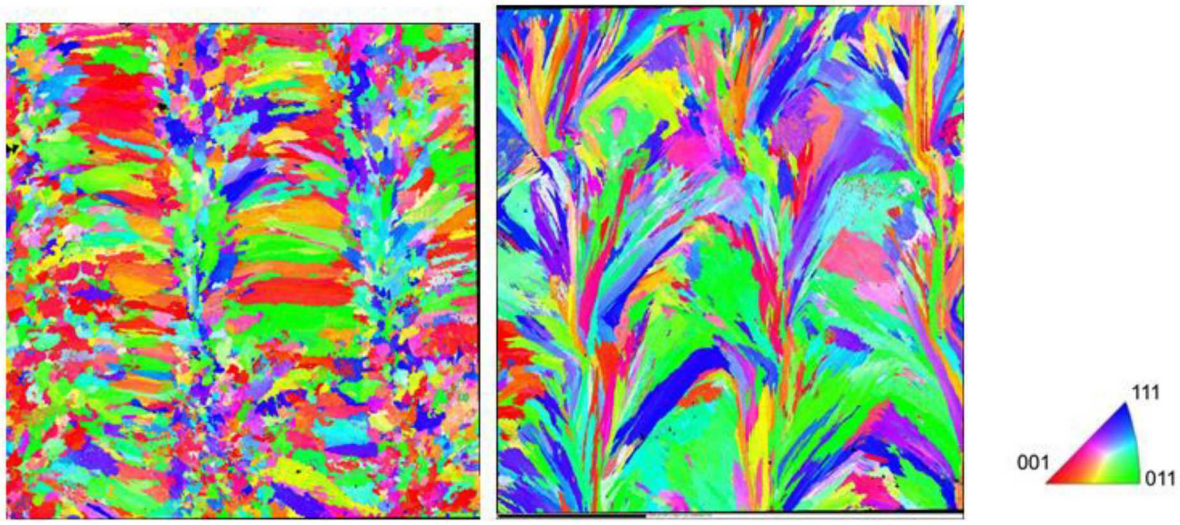

Figure 2-4. EBSD maps of AM stainless steel 304L made using a laser power of 3.8 kW implementing an alternating, 90°-rotated scan fabrication method for the Z-Cut AM (Left) and X-Cut AM (Center). The EBSD maps display the austenite grain structure of the deposited material, as indicated by the color map (Right). Ferrite or non-indexed austenite is black. For the Z-Cut image (Left) the laser scan direction (X) is vertical. For the X-Cut image (Center) the build direction (Z) is vertical. Example was taken from PSU build 20B.

Other microstructural features are evident. Sub-micron wide, round features are found throughout the AM stainless steel with no obvious preferred locations such as sub-grain boundaries. Only evident in SEM images, these features form with a particle-to-particle spacing that is several microns. These features often appear bright in the SEM. These objects are likely oxide dispersions. Small oxide particles can form during AM due to reaction of laser heated metal with oxygen contained within the feedstock (likely incorporated in the powder particles as an oxide film) or residual oxygen contained within the Ar purged vessel. Oxygen may enter the chamber as a trace impurity of the ultra-high purity Ar gas or be evolved by heating of internal components. Regardless, the microstructure maps suggest the AM material is fully dense.

3. COMPUTATIONAL FRAMEWORK

The goal of the computational effort is to develop capabilities for understanding microstructure effects on the dynamic response of AM materials. This includes upscaling strategies to facilitate microstructure-aware simulations, model development for spall response, and model validation; model validation is discussed in Section 5 of this report.

3.1. Upscaling AM Microstructure Morphologies

It is well known that strength properties and response of materials is dictated by material microstructures [11, 13]. The microstructures of the wrought and AM 304L SS are depicted in Figure 2-1 and Figure 2-4, respectively. Microstructural morphologies, spatial heterogeneities, and length scale differences between wrought and AM 304L SS are apparent.

To facilitate modeling of AM materials, an upscaling approach was developed. Conceptual objectives of the upscaling strategy are listed below.

- Avoid vexing problem of meshing material details.
- Systematically represent properties on coarse continuum model.
- Respect microstructural morphologies and associated length scales.
- Reflect microstructure heterogeneity and AM material variability.

The approach used to systematically represent properties on a coarse continuum model consists of the following key elements; details of these elements are described elsewhere [14].

- The Stochastic Parallel PARticle Kinetic Simulator (SPPARKS) [15, 16] generated synthetic microstructures based on a model of AM process
- Computation of spatial statistics associated with observation points
- Application of clustering algorithms from machine learning to represent properties on coarse continuum models
- ALEGRA [17] simulation of dynamic response of AM 304L SS using upscaled synthetic microstructure representation

3.1.1. SPPARKS Generated Synthetic Microstructures

Kinetic Monte Carlo (KMC) simulations with SPPARKS are used to simulate the AM process. SPPARKS was successfully used to simulate welding and AM processes [18, 19] and produced representative microstructures. SPPARKS generated synthetic microstructures predict grain size and shape morphologies produced by a particular manufacturing process; microstructure morphologies are process sensitive. A SPPARKS generated microstructure is shown Figure 3-1; this figure also illustrates two observation points $\boldsymbol{r}$ and $\boldsymbol{s}$. Observation points are used for computation of spatial statistics described in Section 3.1.2.

3.1.2. Computation of Spatial Statistics

For the purpose of incorporating microstructural grain morphologies into continuum scale computational codes such as ALEGRA, a strategy was developed to compute an average grain shape for a set of fixed observation points within images. To generate an average shape at a particular observation point, many microstructure realizations must be synthesized; these are generated using SPPARKS AM microstructure simulations. Instead of averaging grain shape across a single image, grain shapes are averaged across multiple microstructure realizations for a set of fixed observation

points, where observation points coincide with quadrature points from a finite element (FE) mesh. Conceptually, a finite element mesh is registered/overlaid with the output from a SPPARKS simulation.

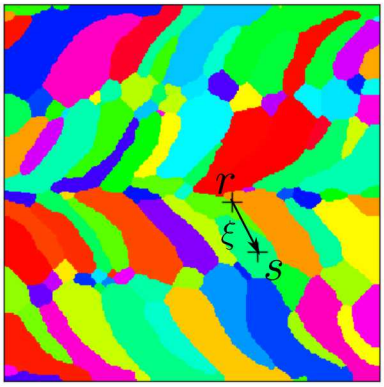

Figure 3-1. SPPARKs generated synthetic microstructure with observation points, *r* and *s*.

On the left side of Figure 3-2, a simulated microstructure for an AM material is shown; overlaid on the microstructure is a square FE mesh with a hole cut out; for dynamic testing, a piece of material, represented by the FE mesh, is cut from the larger piece of AM material. Each FE quadrature point is used as an observation point to collect statistics across many microstructure simulations and is used to construct the most likely microstructure for simulations on the FE mesh.

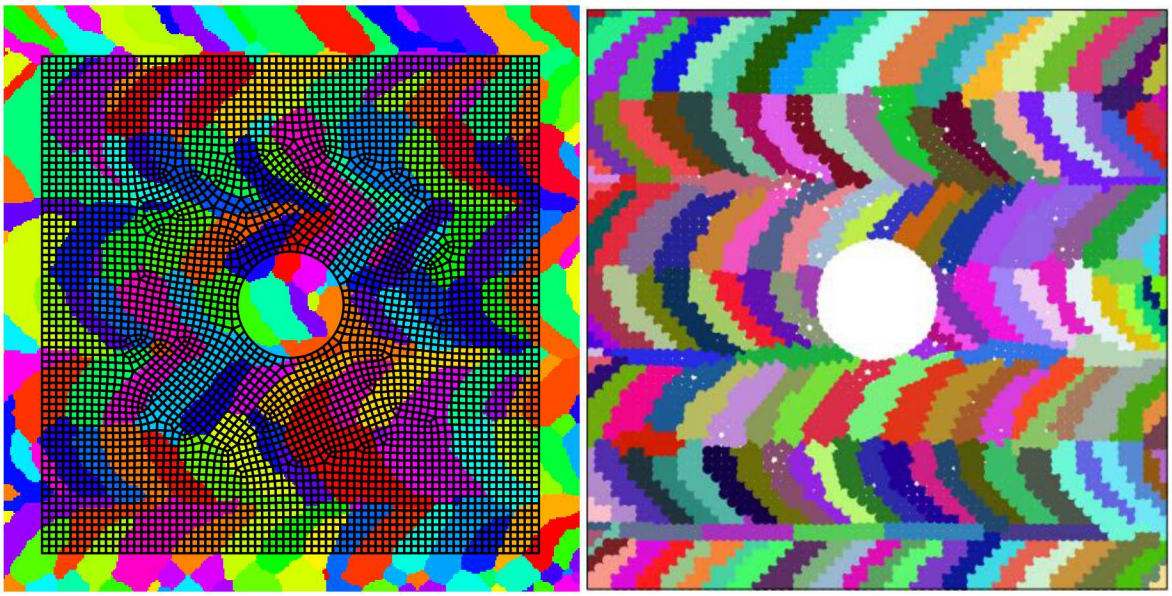

Figure 3-2. Square plate with hole. FE mesh overlay with simulated microstructure (Left). Most likely microstructure representation on FE mesh (Right).

3.1.3. Calculation of Most Likely Upscaled Microstructure

For each SPPARKS microstructure simulation, a FE mesh of interest is overlaid on the resulting microstructure to collect statistics; then spectral clustering algorithms are used to generate the most likely microstructure representation from the FE observation points. Using this process, the most

likely microstructure representation for the square plate with a hole is shown on the right side of Figure 3-2, where different colors denote different grains. When this microstructure is created, a separate exodus file [20] is written for use in simulation codes. For example, ALEGRA reads the exodus file and distributes properties across the FE mesh that reflects length scale and grain morphologies of the underlying AM material and process. This particular case is a numerical example of the upscaling process in development and does not fully represent a validated SPPARKS microstructure simulation of the AM process. That is work planned for the near future.

3.2. Spall Kinetics Model (SKM)

Under this effort, we are developing a computational material and damage model for the response of metals under strong, high-rate tensile loading. This new SKM model has the following distinguishing features:

- It incorporates softening behavior prior to fracture.
- Damage is explicitly time-dependent under loading conditions that lead to fracture.
    - This time dependence leads to a rate effect on spall strength.
    - It also leads to better agreement for reproducing certain details of experimental data.
- It is designed to be applicable to any equation of state (EOS) in a hydrocode (Mie-Gruneisen [21], tabular, analytic, etc.) although it has only been tested with Mie-Gruneisen EOS to date.
- It contains input parameters that can be calibrated to reflect the differences between AM and conventional materials.
- It can be applied within detailed computational models of the microstructure and failure progression as well as homogenized hydrocode simulations.
- It works in conjunction with any strength model in a hydrocode (J_2 elastic-plastic, Mohr-Coulomb, anisotropic, etc.).
- It accounts for the possible effect of embrittlement due to a (strongly compressive) shock wave on subsequent (tensile) spall failure.

3.2.1. Motivation for SKM Development

For short periods of time, many metals can sustain tensile stress far in excess of what would be measured under static conditions. Effects such as this help to determine the performance of materials under shock wave loading. They can also manifest themselves differently according to the microstructure and processing conditions of the material.

The spall behavior of metals is typically modeled in finite-volume hydrocodes, such as CTH [22], and/or arbitrary Lagrangian Eulerian (ALE) hydrocodes, like ALEGRA, with a simple pressure or stress cutoff. With this method, when a prescribed tensile failure pressure/stress is exceeded in a cell, void is inserted, and the material "fails". The simplest assumption, which is the default in CTH, is that this failure pressure/stress is independent of rate or other conditions.

An alternative way of modeling material failure that is available in standard CTH and ALEGRA is the Johnson-Cook (JC) fracture model [23], which explicitly incorporates strain rate dependence in the failure strain. This model uses equivalent plastic strain as the key index for material failure. The critical plastic strain for failure is weighted according to the current hydrostatic stress as well as the rate of deformation.

The performance of these standard models, the simple pressure cutoff and the JC fracture model, is illustrated in a typical spall application in Figure 3-3. This plate impact experiment is designed to produce a spall surface near the center of the specimen [24]. The figure compares the measured velocity history, recorded with a velocity interferometer system for any reflector (VISAR) [25], of the rear surface of a conventionally wrought 304L SS specimen with three computational models: (left) simple 3.5 GPa stress cutoff determined from spall strength measurements [24], (center) the current calibration of the JC fracture model for S7 tool steel [26], and (right) SKM. S7 tool steel was deemed an appropriate substitute for 304L SS. All of the computations used the JC *plasticity* model [27].

Following the arrival of the initial shock wave at the free surface, all the details of the free surface velocity history are determined by the process of spallation in the interior of the sample. From the results shown in Figure 3-3, the SKM more accurately reproduces the nuances of the spall process over existing calibrated models. While it is possible to recalibrate the stress cutoff and JC fracture approaches to achieve better agreement with the data, the results shown in Figure 3-3 suggests their formulations are not representative of the physical processes of spall.

Further examples, showing the ability of the SKM to represent the behavior of both wrought and AM 304L SS, are given in Section 5.2.

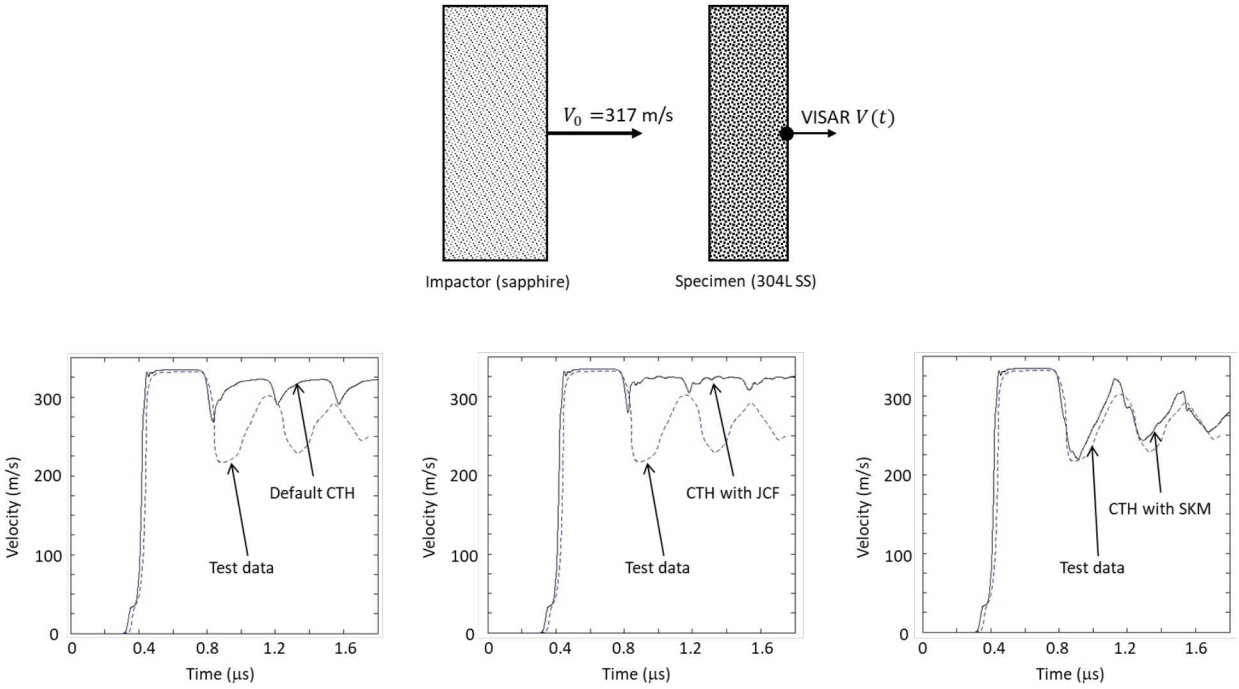

Figure 3-3. Comparison of spall test data [24] with three computational spall models. Left: simple stress cutoff. Center: JC fracture model. Right: present work (SKM).

3.2.2. SKM Theory

The details of the SKM model are described in [28]. Here, we give a summary of its basic features.

It is assumed that for each cell in CTH (or element in ALEGRA) there is some pressure that emerges from the EOS as a function of the local mass density and internal energy density (or

equivalently the temperature). Call this pressure the EOS pressure, denoted by P_{EOS}. The SKM model modifies this EOS pressure to incorporate dynamic tensile failure.

The model defines an *undamaged pressure* U that characterizes an assumed softening as the EOS pressure becomes more strongly tensile over time. This softening is found to be a necessary ingredient in reproducing the data in experiments like the one shown in Figure 3-3. The undamaged pressure is computed as a function of the EOS pressure as shown in Figure 3-4. The asymptotic limit of U for strongly hydrostatic EOS pressure depends on the volumetric strain rate in the cell and is denoted by Q.

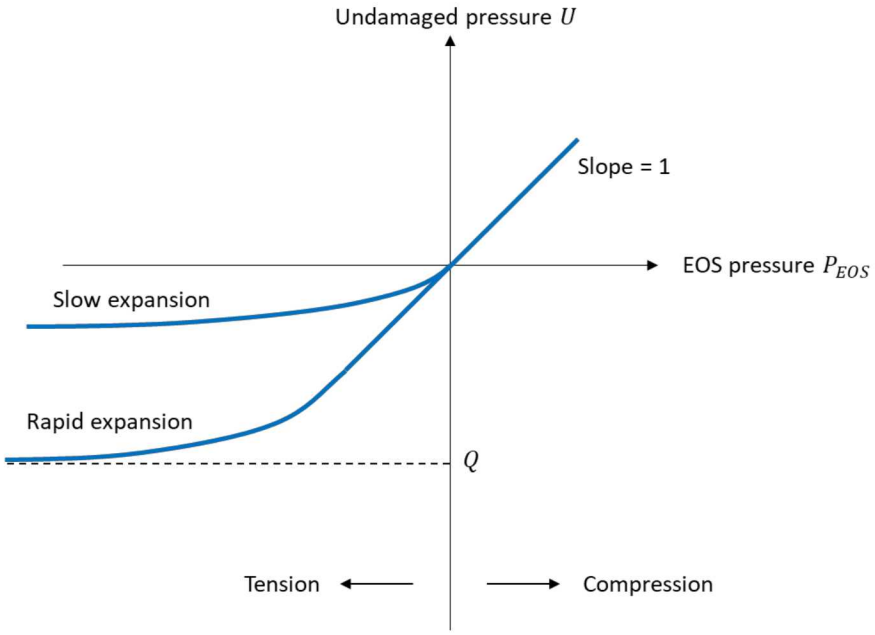

Figure 3-4. Undamaged pressure as a function of EOS pressure in the SKM model.

Damage accumulates when the EOS pressure is more strongly tensile than RQ, where R is a user input parameter less than 1. While this condition is met, the damage $F(t)$ in the cell grows at a constant rate that is a function of the maximum compressive stress that the cell has experienced up to that time. This dependence accounts for the microstructural changes that are left in the wake of a strong shock wave that can lead to embrittlement under tension. The growth of damage can be written in the form

$$\dot{F}(t) = C(P_{max}), \quad \text{if } P_{EOS} < RQ, \;\; 0 \le F(t) \le 1$$

where P_{max} is the maximum pressure (e.g., due to a shock wave) that was present in the cell up to the time t. As shown in Figure 3-5, a cell under sufficiently strong tension, at a constant rate of volumetric strain, has its pressure reduced in magnitude to zero over time. The purple lines show the drop in tensile cell pressure over time, as the material continues to expand. The stress is decreased according to the relation

$$P = \big(1 - F(t)\big)U$$

where P is the cell pressure, which is the output from the SKM model. The rate of the decrease in stress is higher for material that has undergone strong shock loading. If J_2 flow theory is used in the strength model, the flow stress is reduced by the same linear dependence on damage.

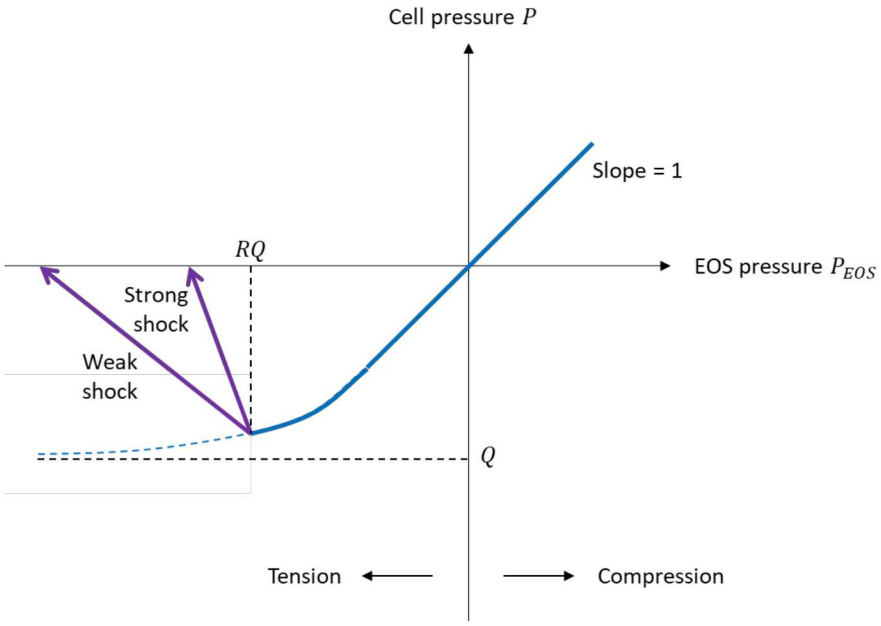

Figure 3-5. Damage growth reduces the cell stress.

The way that SKM treats damage growth, as a function of time rather than rate, tends to be supported by experiments suggesting that SS can sustain larger tensile stress for short time intervals than longer time intervals [29]. The SKM model results with CTH are also largely consistent with detailed two-dimensional models using peridynamics that show the evolution of damage growth in a plate impact experiment (Figure 3-6). The microstructural model shows the finite period of time required from initiation to completion of the failure progression leading to spall. Figure 3-7 compares the microstructural and SKM results for free surface velocity, showing a number of similarities. In both simulations, the amplitude and shape of the oscillations after the initial spall signal are affected by the finite rate of damage accumulation. It is also of interest that there is not a clean break between the spall surfaces; some material remains as a bridge between these surfaces. This bridge material also affects the amplitude of the free surface oscillations.

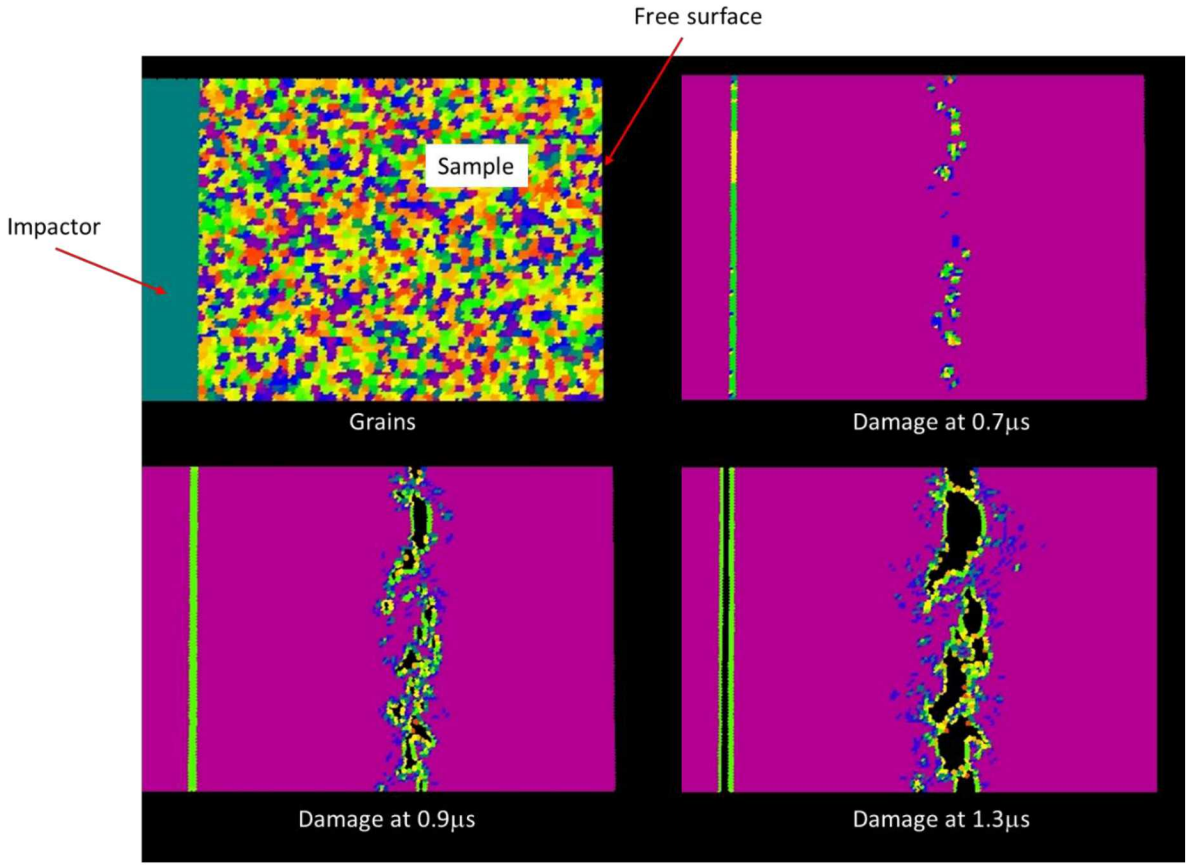

Figure 3-6. Microstructural peridynamic simulation of a plate impact experiment resulting in spall.

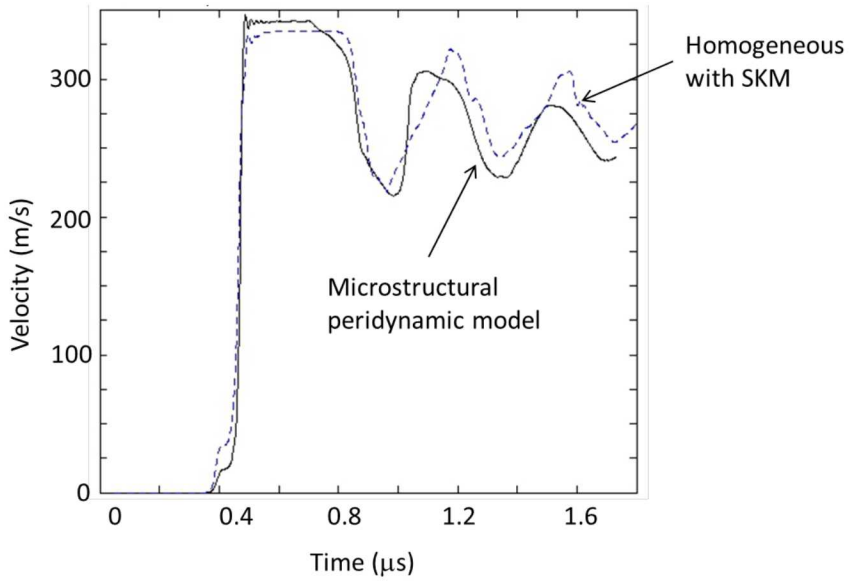

Figure 3-7. Comparison of SKM and detailed microstructural simulations for free surface velocity with an impact velocity of 317 m/s.

4. EXPERIMENTAL INVESTIGATIONS ON 304L STAINLESS STEEL

The experimental work focused on characterizing the response of the X-Cut and Z-Cut AM 304L SS relative to a conventionally wrought processed 304L SS under high pressure, high strain rate loading. Two types of dynamic compression techniques were used: pulsed power and projectile impact. The results obtained with each experimental technique are discussed below.

4.1. Pulsed Power Experiments

Pulsed power experiments were performed to study the shockless, or ramp, compression on both wrought and AM 304L SS to pressures exceeding 1 Mbar (100 GPa). Shockless compression produces high pressures, but relatively low temperatures relative to shock compression. This means the loading path under shockless compression more closely approximates a material isentrope [30], instead of the Hugoniot. Additionally, the release behavior from high pressure in a shockless compression experiment provides a measure of the flow strength [13, 31]. In this work, experiments employing shockless compression followed by release, termed ramp-release experiments, were performed on the Sandia National Laboratories pulsed power machines Z [32, 33] and Thor [34].

4.1.1. Ramp-Release Experiments on the Z Machine

A total of seven dedicated Z experiments were performed on AM and wrought 304L SS to study the EOS and flow strength near Mbar pressures. All experiments employed a stripline target assembly, as shown in Figure 4-1. The stripline geometry uses two parallel panels separated by an anode-cathode, or AK gap, that are shorted at the top. Application of a time-varying current pulse to the shorted load, generates a time-varying magnetic field in the AK gap. The resulting Lorentz force induces a pressure wave normal to the panels. This stress wave propagates ahead of the magnetic diffusion front, enabling the measurement of the mechanical response of the material at high pressure. In a stripline geometry, the magnetic field is the same at identical locations along the height of anode and cathode panels if the geometric asymmetries between panels (i.e. deformation) is minimal.

For this work, both the anode and cathode were made of Cu with a nominal 2 mm floor thickness. The anode panel contained three 304L SS samples along its height, each being roughly a 15 mm square and nominally 1.5 mm thick. The thicknesses and type of each 304L SS sample are given in Table 4-1. Each sample was backed by a nominally 6 mm thick LiF [100] window. The LiF window had a 2500 angstrom Al coating on the sample side and an anti-reflective coating for 532 nm light on the free surface to improve the interferometric data returned. The cathode panel contained three LiF windows mounted opposite each 304L SS sample to provide a cathode, or drive, measurement. A drive measurement enables the back calculation of the applied magnetic field [35, 36]. Having a drive measurement opposite each sample enables correction for variations in magnetic field along the panel height [37]. In all experiments, the magnetic field imparted on the cathode was identical to that on the anode during the timescale of interest, as verified by 2D magnetohydrodynamic (MHD) calculations in ALEGRA.

Each location along the anode and cathode panels was monitored with VISAR, employing up to 3 independent velocity per fringe (VPF) constants.

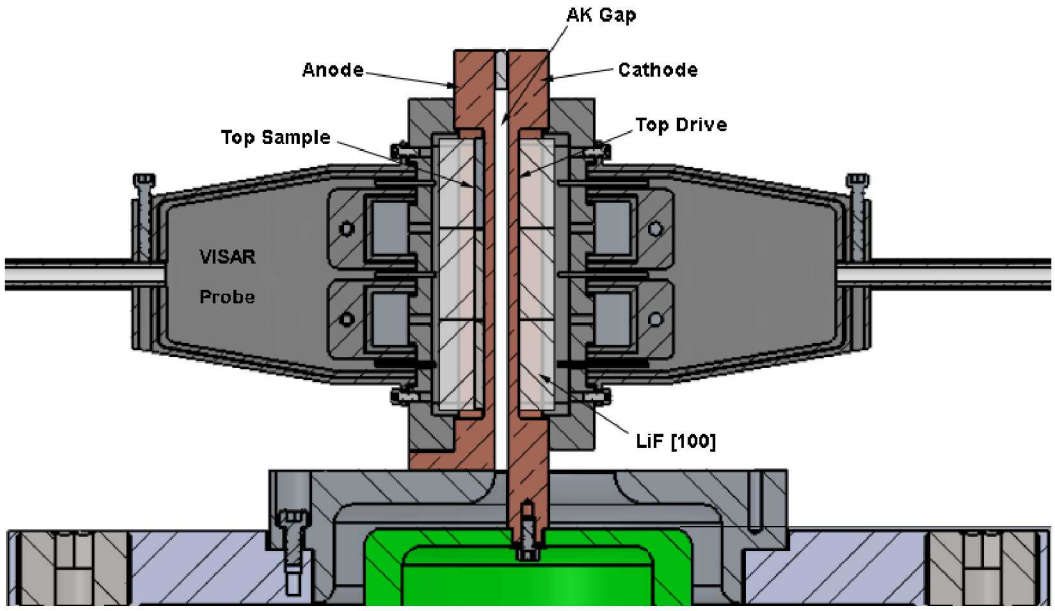

Figure 4-1. Schematic of the stripline Z experiments. The stripline geometry contains three samples under measurement on the anode while the cathode contains three drive measurements opposite each sample.

Table 4-1. Thicknesses in mm of all Z experiment 304L SS samples along with 95% confidence bounds

Experiment	Bottom Anode Sample*	Middle Anode Sample*	Top Anode Sample*
Z3090	1.465 ± 0.006 (W)	1.457 ± 0.002 (X)	1.493 ± 0.013 (Z)
Z3113	1.513 ± 0.014 (Z)	1.518 ± 0.009 (Z) Heat treated at 750C	1.514 ± 0.004 (Z) Heat treated at 1050C
Z3129	1.482 ± 0.012 (W)	1.497 ± 0.012 (X)	1.482 ± 0.003 (Z)
Z3187	1.489 ± 0.008 (X)	1.502 ± 0.002 (Z)	1.490 ± 0.005 (W)
Z3257	1.486 ± 0.005 (X)	1.497 ± 0.006 (Z)	1.495 ± 0.006 (W)
Z3324	1.491 ± 0.006 (X)	1.504 ± 0.005 (Z)	1.502 ± 0.004 (W)
Z3340	1.494 ± 0.006 (X)	1.499 ± 0.005 (Z)	1.500 ± 0.007 (W)

*W represents a wrought 304L SS sample, X represents an X-Cut AM 340L SS sample, and Z represents a Z-Cut AM 304L SS sample

4.1.1.1. Preliminary Results of the Ramp-Release Experiments on Z

Figure 4-1 shows the interface velocity recorded for each as-built Z-Cut AM 304L SS sample in the Z experiments, arbitrarily shifted in time for clarity. Once the magnetic field was calculated from the drive measurements, the interface velocity between the sample and window was analyzed using inverse Lagrangian analysis (ILA) employing a transfer function method [13, 30, 31] to determine

the quasi-isentrope and flow strength. A detailed description of the analysis method for ramp-release experiments is located elsewhere [13, 30, 31].

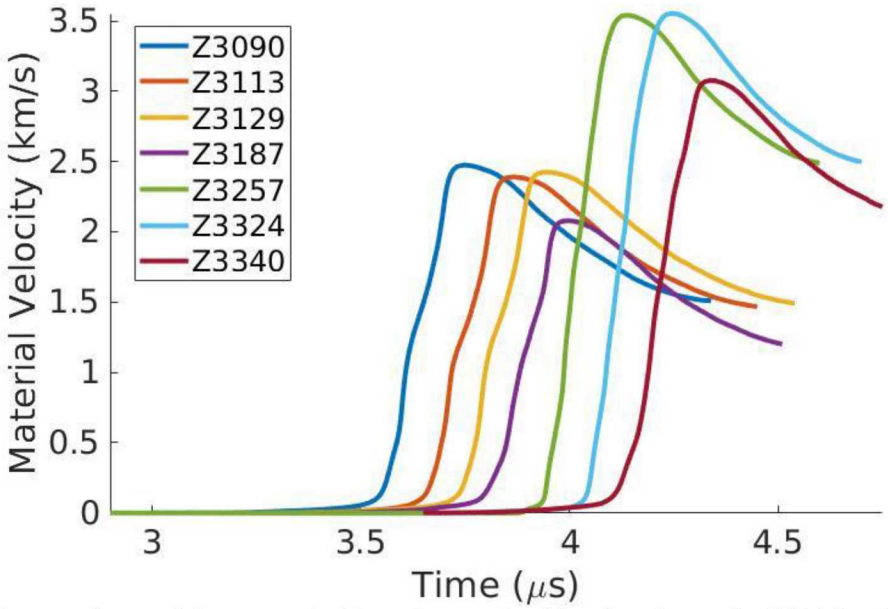

Figure 4-2. Comparison of the recorded interface velocities for the as-build Z-Cut AM 304L SS sample. The profiles are arbitrarily shifted in time for clarity.

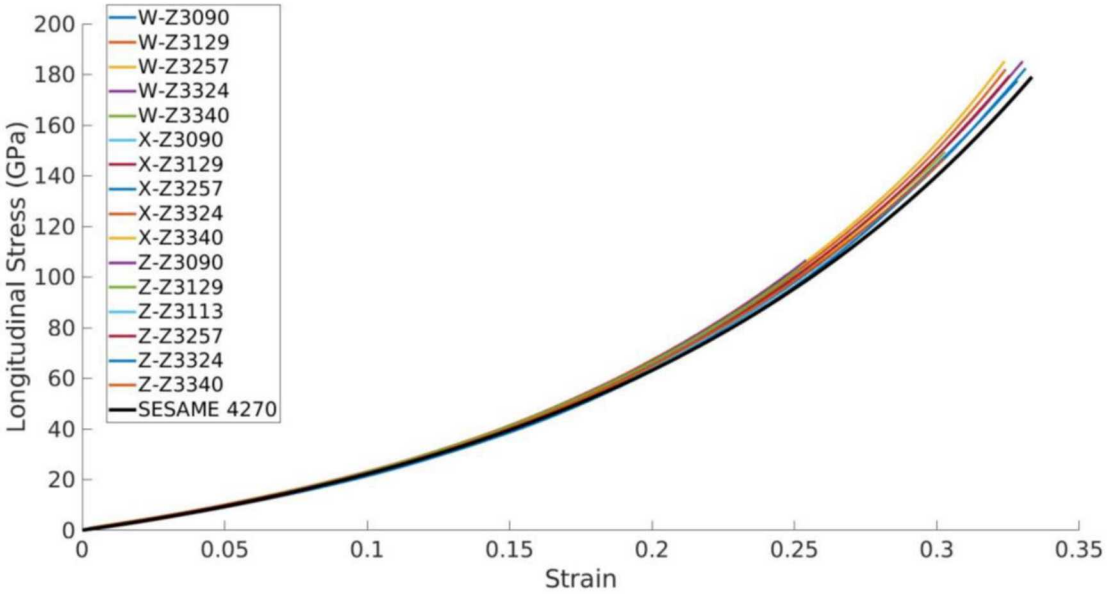

Figure 4-3. Preliminary quasi-isentropes for all wrought and as-built AM 304L SS samples along with the SESAME 4270 isentrope. Here, W refers to the wrought sample, X to the X-Cut sample, and Z to the Z-Cut sample. The AM and wrought 304L SS exhibit similar quasi-isentropic compression up to 2 Mbar, which is stiffer than that predicted by the SESAME 4270 table.

The preliminary quasi-isentropes the wrought and AM 304L SS samples for the Z experiments, except Z3187, are shown in Figure 4-3. The quasi-isentropic compression of both orientations of

the AM 304L SS follows that of the wrought material up to 2 Mbar. Figure 4-3 also shows the isentrope from the 4270 SESAME table, which was built for 304L SS using prior Hugoniot data [38]. The observed behavior of the both the wrought and AM material is stiffer than that predicted by the SESAME 4270 table.

The preliminary flow strengths extracted from select Z experiments is presented in Figure 4-4. Also shown in Figure 4-4 are flow strengths obtained in this work using lower pressure ramp-release experiments on Thor and plate impact experiments at STAR, which are discussed in Sections 4.1.2 and 4.2.1.1, respectively. The results obtained in this work are compared to values previously obtained using quasi-static compression tests and plate impact experiments [11] along with the current calibration of the Steinberg-Guinan (SG) model for 304L SS [39]. The results show that the current calibration of the SG model for 304L SS, while accurate at low pressures (< 10 GPa), underpredict the flow strength at high pressures. This trend has been identified in other metals, like tantalum [40].

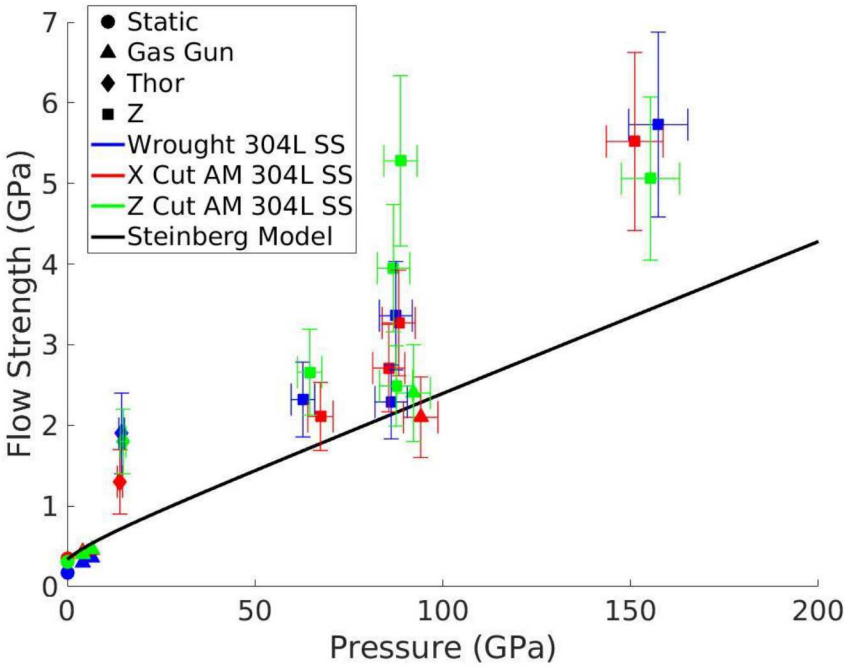

Figure 4-4. Flow strength measurements of wrought and AM 304L SS. Circles represent prior quasi-static experiments [11]. Triangles represent prior low pressure plate impact experiments [24] and the higher pressure plate impact experiments of this work. The diamonds and squares represent preliminary values obtained from ramp-release experiments on Thor and Z, respectively. Blue results represent wrought material, red results the X-Cut AM, and green results the Z-Cut AM. The flow strengths are compared to the current SG model for 304L SS [39]. While the current calibration of the SG model does well at low pressures (< 10 GPa), it underestimates the flow strength at higher pressures.

The results of the ramp-release experiments also show little variation in the response of the AM orientations relative to the wrought data. However, the limited number of data points makes definitive conclusions difficult. Near 1 Mbar, there are three measurements of the Z-Cut AM 304L SS. Two measurements are in close agreement, but another is significantly higher. This suggests sample-to-sample variability in the Z-Cut AM material. Given the complexity in the microstructure shown in Figure 2-4, it is not unreasonable to think this sample-to-sample variability is

microstructurally driven. The grain size in this orientation (~ 1mm) is on the order of the sample thickness (~ 1.5 mm), hence the material sample is morphologically heterogeneous at this length scale. Further analysis of this data and additional experiments are underway to reduce uncertainty and determine the extent that microstructure influences the flow strength.

4.1.2. Ramp-Release Experiments on Thor

Thor is a compact pulsed power machine located at the Dynamic Integrated Compression (DICE) facility and is capable of reaching peak pressures of ~20 GPa in ramp-release experiments [34]. While the configuration of ramp-release experiments on Thor follows that of Z, outlined in Section 4.1.1, its smaller size limits the number of samples per panel to 1. This minimizes load inductance and maximizes the attainable peak pressure. Two types of Thor experiments were performed in this work: input/output (IO) and sample A/sample B (AB) configurations. The IO configuration is analogous to the Z experiments described earlier and follows the same analysis procedure as outlined in Section 4.1.1. The IO configuration contains a sample on the anode panel and a drive measurement on the cathode panel. IO configuration is ideal for performing forward simulations and obtaining quantitative estimates of the flow strength. The AB configuration consists of samples of nearly identical thickness, but varying microstructures (i.e. wrought, X-Cut AM, or Z-Cut AM) on each electrode. The AB configuration is well-suited to a qualitative assessment of differences in the material response.

4.1.2.1. Preliminary Results of the Ramp-Release Experiments on Thor

The ramp-release experiments on Thor were done in two stages. The first using single-point velocimetry to establish base-line behavior. The second employed a multi-point diagnostic configuration to increase data return and quantify spatial variation in the response of AM 304L SS.

Table 4-2. Summary of the single point Thor experiments.

Experiment	Configuration	Anode Sample Thickness (mm)*	Cathode Sample Thickness (mm)*	Mean Pressure (GPa)	Flow Strength (GPa)
Thor-22	IO	0.9828 (X)	Drive	14.0 ± 0.7	1.3 ± 0.4
Thor-26	IO	1.0456 (W)	Drive	14.5 ± 0.7	1.9 ± 0.5.
Thor-27	IO	1.0755 (Z)	Drive	14.9 ± 0.7	1.8± 0.4
Thor-28	AB	1.0479 (W)	1.0465 (Z)	NA	NA
Thor-29	AB	1.0458 (W)	1.1112 (X)	NA	NA

*W represents a wrought 304L SS sample, X represents an X-Cut AM 340L SS sample, and Z represents a Z-Cut AM 304L SS sample

4.1.2.1.1. Ramp-Release Experiments with Single-Point Velocimetry

A total of five ramp-release experiments using single-point velocimetry were performed on Thor. Each experiment used a 10 mm wide Cu panel with an 8 mm diameter sample. Experimental details are summarized in Table 4-2. All samples were backed with a nominally 6 mm thick LiF window. All windows had a 2500 angstrom Al coating on the sample side and an anti-reflective coating for 532 nm light on the free surface to improve the interferometric data returned. Each experiment recorded one dual-VPF VISAR measurement and two photonic Doppler velocimetry (PDV) [41]

measurements at the center of each sample/drive. The four independent velocimetry measurements were generally averaged to provide the best estimate of the interface velocity, using their respective uncertainties as weights.

A comparison of the average velocimetry response of the AB experiments is given in Figure 4-5, and illustrates some qualitative observations. The differences at early times (< 1.25 μs) are related to the initial yielding of the samples. The higher velocities correspond to higher yield strengths. Both the X-Cut and Z-Cut samples exhibit higher initial yield strengths than the wrought material, which is consistent with the quasi-static data [11]. Most of the loading and unloading portions of the velocity profiles are primarily sensitive to the EOS, so there is no measurable differences in the hydrostatic compression responses. Finally, the sensitivity to the strength at the peak loading state manifests in the region around the velocity reversal. As illustrated, slight differences are observed. In this case, the trend is opposite the initial yielding: lower velocities correspond to higher strengths. Thus, the X-Cut and Z-Cut samples exhibit higher strength than the wrought samples under ramp compression to ~15 GPa.

The IO experiments are summarized in Table 4-2 and the extracted flow strengths shown in Figure 4-4. The overall trends are not consistent with the AB experiments, but the uncertainties are too large to make any definitive statements. The relative cost of a Thor shot makes performing repeat experiments a possibility to drive down these uncertainties and make better quantitative assessments.

Figure 4-5 also shows a pull back signal at late time (> 1.6 μs) after release. This pull back is due to spallation in the sample material. Both past gas gun experiments [24] and preliminary upscaled simulations, described in Section 5.1, have indicated a microstructural dependence on spall strength. The dependence of microstructure on failure strength of the AM material will be explored in more depth in the future.

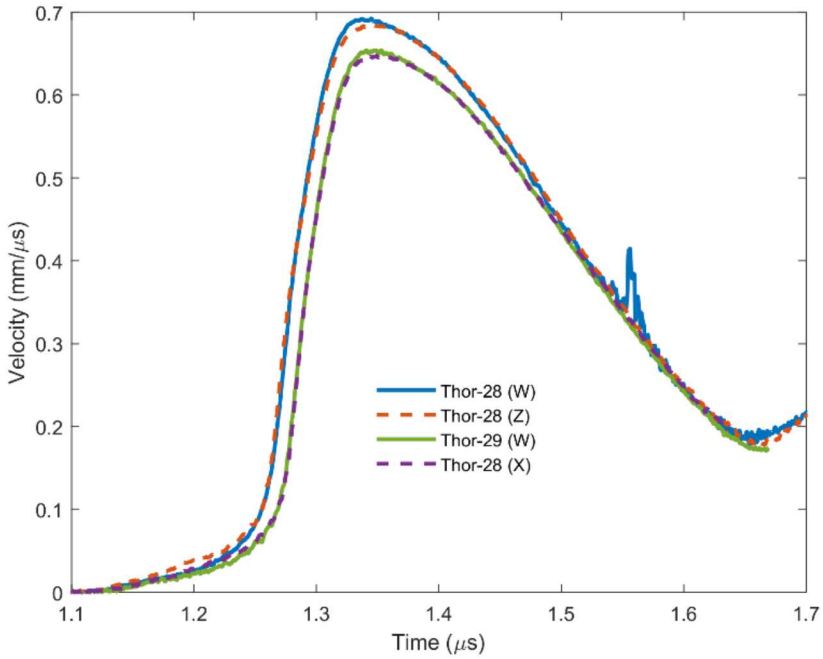

Figure 4-5. Interface velocity measurements from the AB Thor experiments. Clear differences are seen in elastic precursor, velocity near peak, and the pull back signature.

4.1.2.1.2. Ramp-Release Experiments with Multi-Point Velocimetry

To further help in understanding the variation in response of the AM 304L SS during a ramp-release experiment, a multi-point PDV configuration was developed. This allowed for experimental quantification of the velocity variations along the back surface for direct comparison to our microstructurally-aware computational predictions. While several iterations of the multi-point PDV arrangement were applied, this section focuses on the most recent, and most advanced, application.

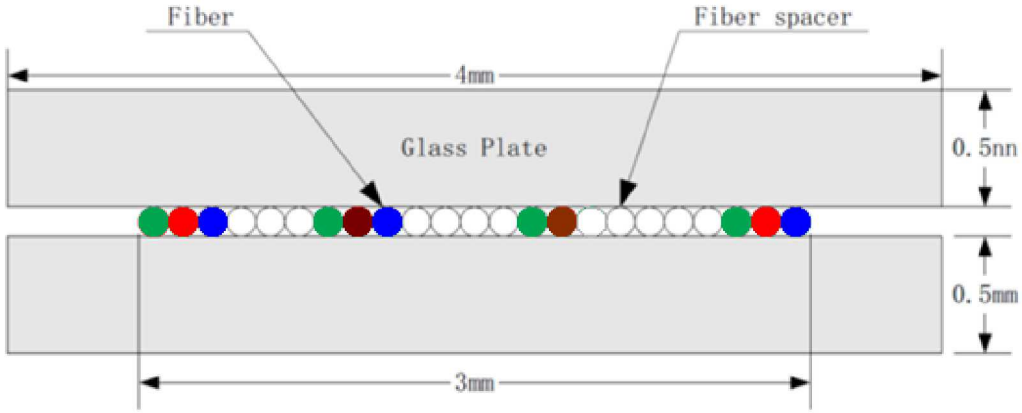

Figure 4-6. A schematic of the PDV fiber array used for the multi-point measurements. The fibers used to illuminate the target are colored red. Each shade of red represents a different wavelength. The return fibers used are colored green and blue to identify different references wavelengths.

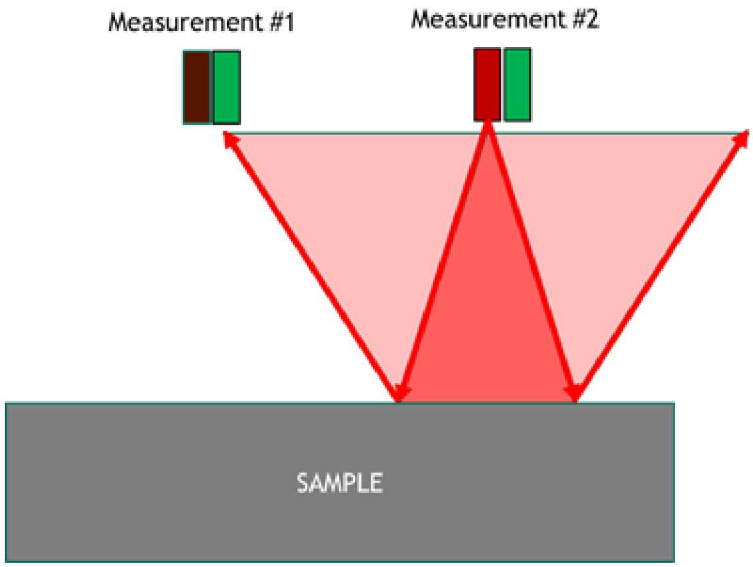

Figure 4-7. Schematic illustrating cross-talk in the multi-point PDV measurements.

The DICE facility has 8 PDV channels available for Thor experiments. In IO experiments, this allows for up to 7 PDV channels on one side while still having an opposing drive measurement to estimate relative timing errors. A commercially available fiber array was used that had 4 measurement locations separated by 1 mm. A schematic of the fiber array is shown in Figure 4-6. The back surface of the sample was illuminated at each location by a send fiber, colored red in Figure 4-6. Three different lasers were used to illuminate the target, each with a different wavelength, represented by different shades of red in Figure 4-6. Each send has two available return

fibers next to it. The return fibers used in the experiment are colored green and blue in Figure 4-6. The different colors of the return fibers indicate separate systems having unique reference wavelengths and recorded on different oscilloscopes.

The use of multiple wavelengths for sends and references was done to differentiate the recorded measurements and increase data return. Given the divergence angle of each send fiber and the 6 mm thick LiF window used in each experiment, cross-talk was inevitable between adjacent channels. Using different wavelengths for sends and returns enabled each measurement combination (i.e. send and return) to have a unique initial beat frequency. Given the relative low velocity expected in the experiment and the bandwidth of the recording oscilloscope, these PDV signals were frequency multiplexed [42], such that no overlap occurred during the experiment. Thus, the number of possible velocity records recorded at the sample/window interface per experiment is 17. Since the measurement surface was specular, the cross-talk measurements correspond to the midpoints between sends, as shown schematically in Figure 4-7. This improves the measurement statistics and helps account for drop outs.

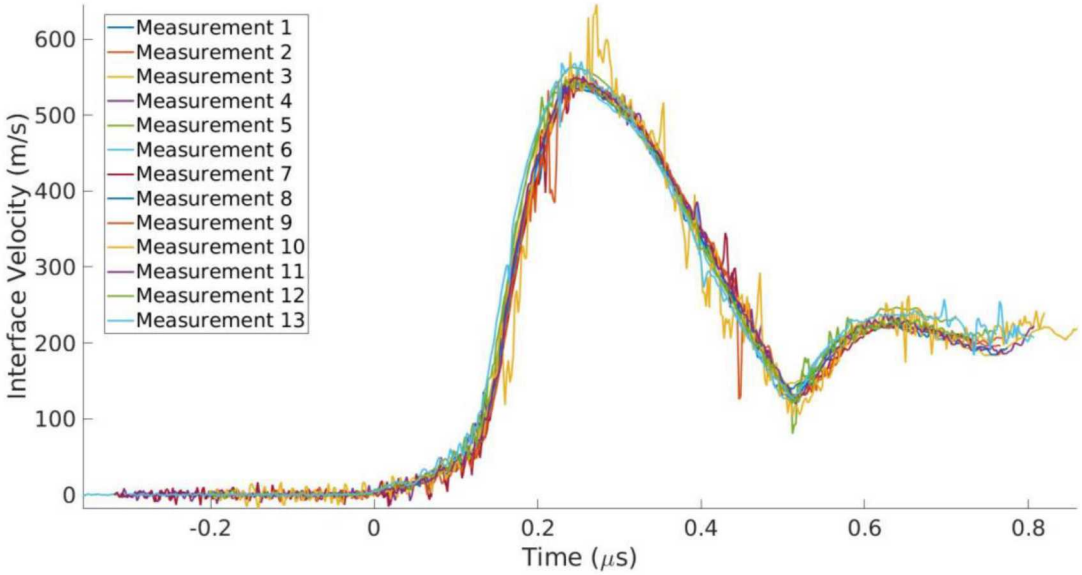

Figure 4-8. Plot of all X-Cut AM/LiF interface velocity histories recorded in the multi-point PDV Thor experiment.

Our first multi-point experiments utilized low powered (40 mW) send lasers. These low powered lasers did not provide enough light for cross talk to be reliably recorded in the experiments. Subsequent experiments utilized two high powered lasers and an amplified low power laser as the sends. All sends illuminated the target with 200 to 250 mW. Figure 4-8 shows all the sample/LiF interface velocity histories recorded in a multi-point PDV Thor experiment on an X-Cut AM sample. Only 13 of the possible 17 measurements were recorded. This was tied to the amplified low power send laser. No cross-talk between this send and any other returns were recorded. Future measurements will utilize three high powered lasers to ensure all possible measurements are recorded. A weighted average of the X Cut AM/LiF interface velocity is shown in Figure 4-9. The weights used were the inverse of the uncertainties of each measurement at a given time. The 95% confidence bound in this weighted average is given by the gray band in Figure 4-9. This distribution

of velocities can be directly compared to computational predictions using our microstructurally-aware framework.

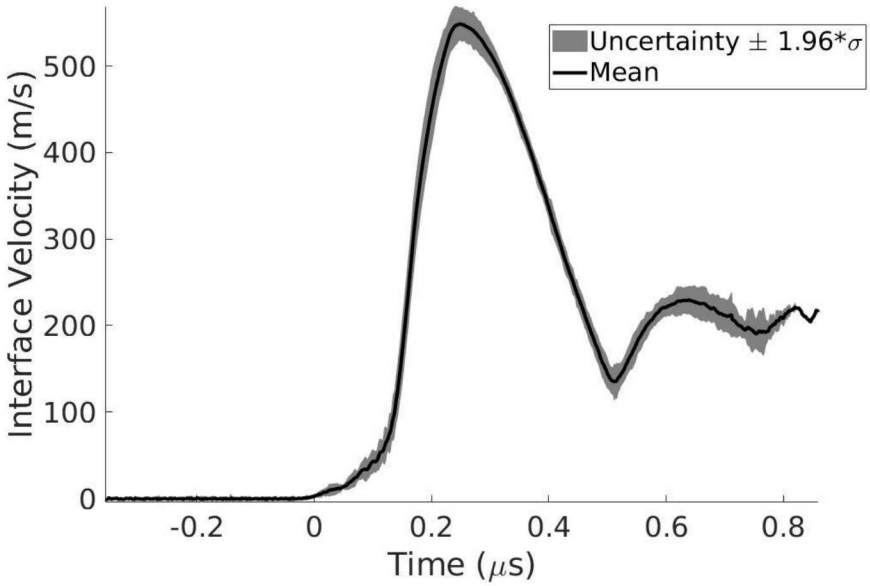

Figure 4-9. Weighted average of the X Cut AM/LiF interface velocity for the multi-point PDV Thor experiment. The inverse of the uncertainty of each measurement at a given time was used as the weight. The gray band represents the 95% confidence bound (±1.96σ) of the average velocity.

4.2. Plate Impact Experiments

Plate impact experiments were performed to obtain flow and failure strength information for wrought and AM 304L SS. The first series of plate impact experiments induced a roughly 1 Mbar shock in the sample material followed by a release, termed a shock-release experiment. These experiments were compared directly to the Z experiments, described in Section 4.1.1, since the quasi-elastic unloading from pressure was used to infer flow strength. The second series of experiments investigated the spallation strength of the wrought an AM material at higher pressures than previously investigated [24] for comparison to the SKM model described in Section 3.2.

4.2.1.1. Preliminary Results of the Shock-Release Experiments

A series of five shock-release experiments were conducted using the 2-stage light-gas gun at the STAR facility. The experimental configuration is illustrated in Figure 4-10. The sample material was used as the impactor and backed by TPX® (polymethylpentene). The impactors were nominally 17 mm in diameter and the TPX® and SS thicknesses were 2 and 2.5 mm, respectively.

This impactor stack was launched on a polycarbonate projectile towards a target plate containing a LiF window at ~5.5 km/s. A 5μm Al buffer, was placed on the impact surface of the LiF window so the interface velocity could be recorded by VISAR. Three PDV probes (AC Photonics) were equally spaced around the window and monitored a retroreflective coating applied to the outside of the sabot to provide an accurate measurement of the impact velocity.

The first three experiments did not return data. For the final two experiments, a 12.7 μm foil was epoxied onto the LiF window as a buffer and resulted in excellent data return. We hypothesize combustion products from the black powder charge accelerated around the projectile and eroded

the 5 μm Al coating prior to impact. The successful experiments are summarized in Table 4-3 and shown in Figure 4-11.

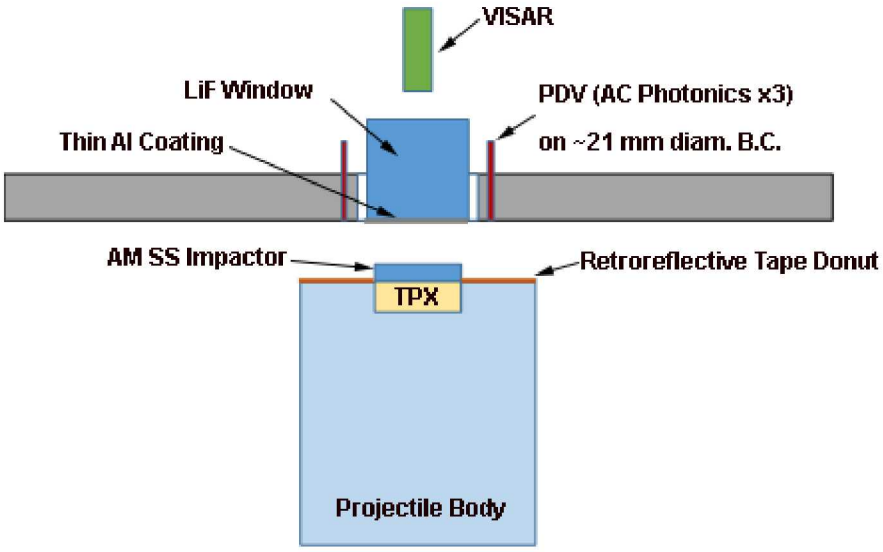

Figure 4-10. Schematic of the shock-release experimental configuration.

Table 4-3. Details of the shock-release experiments.

Experiment	Sample Thickness (mm)*	Impact Velocity (km/s)	Pressure (GPa)	Flow Strength (GPa)
FSI-4	2.4626 (Z)	5.686	92.2 ± 4.5	2.4 ± 0.6
FSI-5	2.4663 (X)	5.630	94.1 ± 4.6	2.1 ± 0.5.

*W represents a wrought 304L SS sample, X represents an X-Cut AM 340L SS sample, and Z represents a Z-Cut AM 304L SS sample

The experiments were analyzed similarly to the Z and Thor experiments. Best-effort simulations, shown in Figure 4-11, were used to perform a window correction and the subsequent Lagrangian analysis to provide quantitative estimates of flow strength. There is a clear elastic-plastic transition following the steady shocked state. The measured flow strength of ~2 GPa matches closely to what was observed in the Z experiments (Figure 4-4). While no significant differences were observed in the measured flow strength under shock-release, there are two few data points to draw definitive conclusions. Experiments are planned for fiscal year (FY) 2020 to reattempt the failed experiments with thicker Al coatings.

4.2.1.2. Preliminary Results of the Spallation Experiments

A pair of impact experiments were conducted to probe the high-pressure spall strength for AM and wrought 304L SS. These tests were performed on the single-stage gas gun at the STAR facility to expand upon earlier results at lower stresses [24].

The experimental configuration utilized for all spall experiments is illustrated in Figure 4-12. With this arrangement, 3 samples (wrought, X-Cut AM, and Z-Cut AM) were simultaneously impacted during each shot by a sapphire disk that was mounted in the projectile nosepiece. VISAR monitored the free-surface motion of each sample. Impact velocities of 0.429 and 0.500 km/s were achieved

for Shots 1G19 and 2G19, respectively. Figure 4-13 provides an overlay of the results for experiments 1G19 and 2G19 with previous spall data obtained on wrought and AM 304L SS [24].

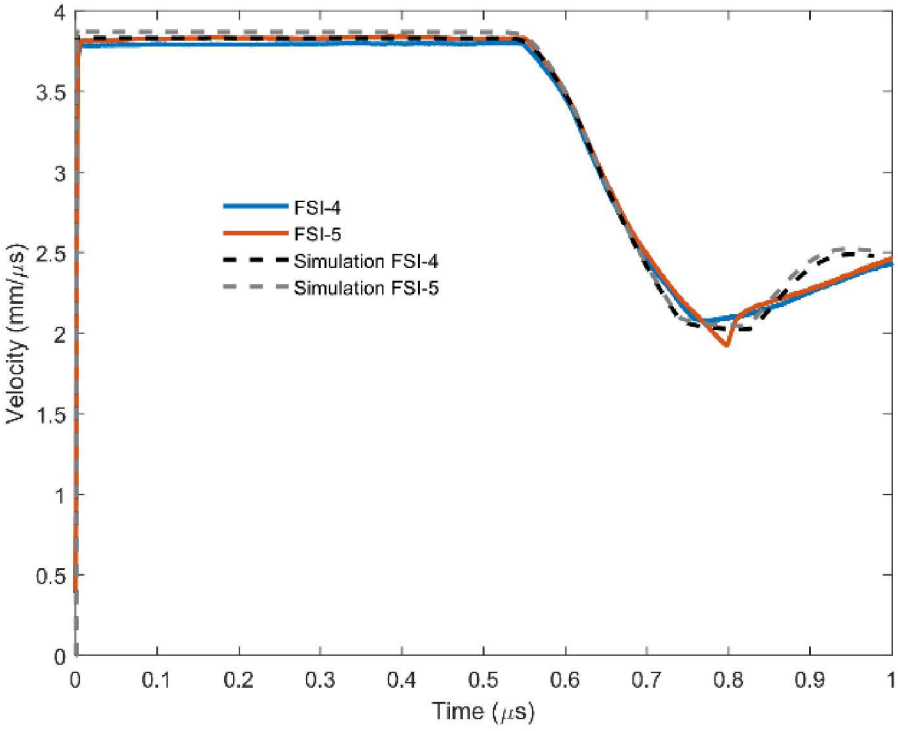

Figure 4-11. Velocity measurements from the shock-release experiments compared to best effort simulations.

Preliminary analysis of the spallation experiments suggests the spall strength of both X-Cut and Z-Cut samples for all impact stresses is consistently higher than that observed for the conventionally wrought material. At high impact stresses, the spall strength of both AM orientations appears to convergence, whereas the spall strength of the Z-Cut AM material exceeds that of the X-Cut material for lower peak stresses. Further analysis of this data and additional experiments are underway to reduce uncertainty and determine the extent that microstructure influences the spallation strength.

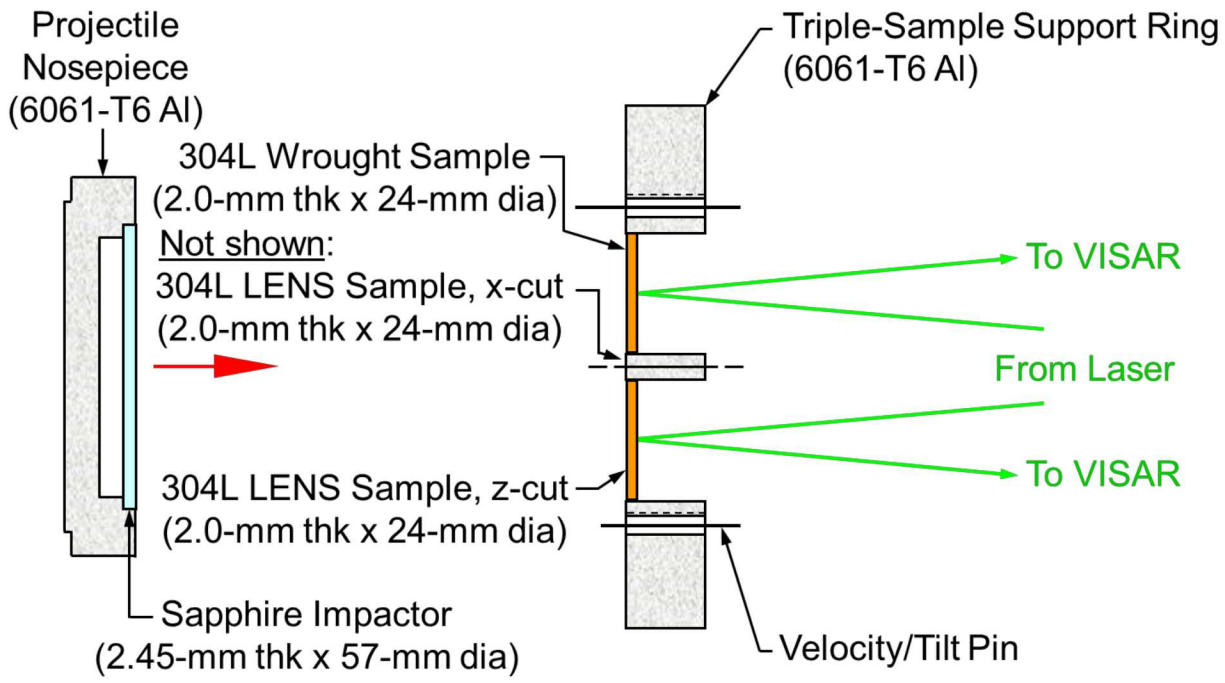

Figure 4-12. Schematic of the spall experiment configuration.

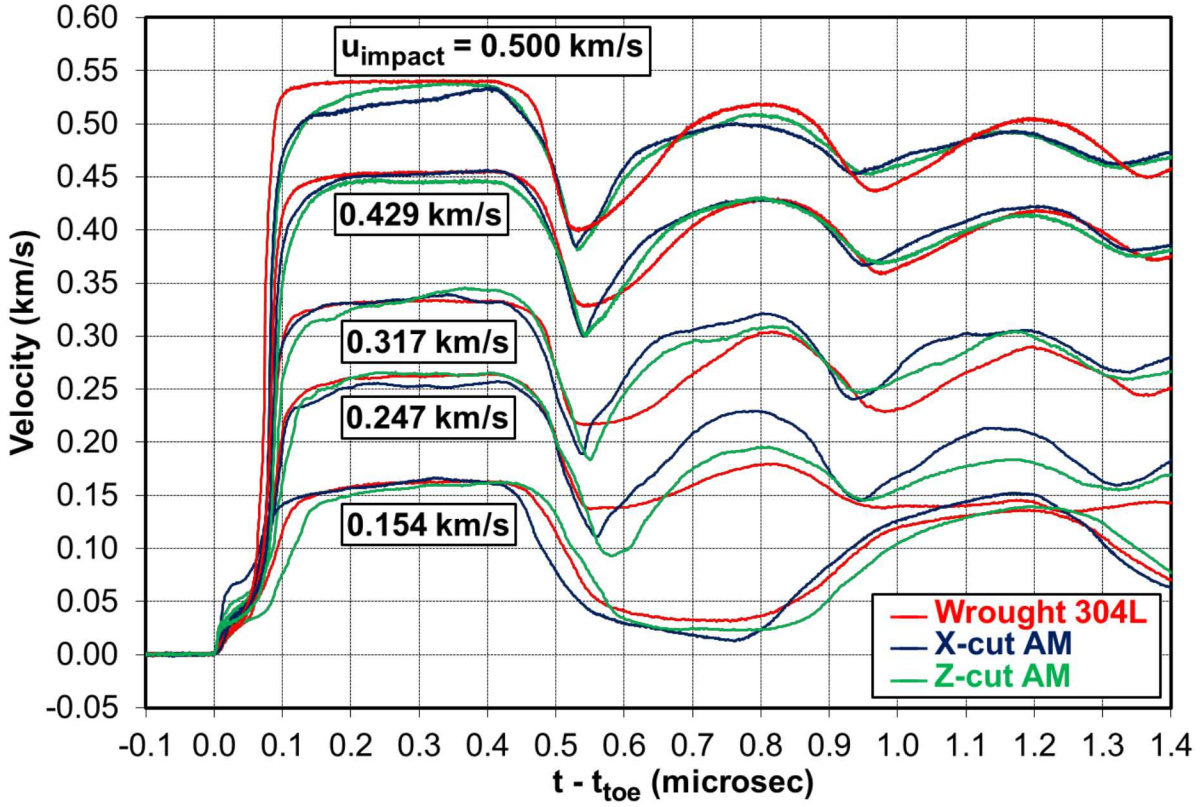

Figure 4-13. Free-surface velocity histories for spall experiments on samples of X-Cut AM, Z-Cut AM, and conventionally wrought type 304L SS. The measured impact velocity is noted for each test. Impact velocities of 0.5 and 0.429 k/s are from this work. Data from the other impact velocities are taken from [24].

5. VALIDATION ACTIVITIES

In FY 2019, a new ALEGRA capability was developed which allows for input of synthetic microstructure representations, as described in Section 3.1.1. This section represents a work in progress with respect to the use of upscaled microstructures in ALEGRA, since this capability was only recently developed. The microstructures used were not validated against microstructures for the materials tested. Nonetheless, these comparisons illustrate the state of the methods and simulation process in development; they also demonstrate the practicality and potential for this approach to upscaling to enable microstructure-aware simulations.

5.1. Microstructural Upscaling

A ramp-release experiment on Thor (Thor-26) was used to demonstrate and develop the ALEGRA capability for reading and using the upscaled representations of AM microstructures. The upscaled representation of the AM material sample is shown in Figure 5-1. The image on the left shows a SPPARKS generated microstructure of an AM material. The left image also shows the FE mesh overlaid for the purposes of extracting spatial statistics and generation of most likely microstructure representation shown in the right image. The image on the right was generated after approximately 150 SPPARKS simulations, such as that shown in the left image. The FE mesh represents a material sample which was cut from a larger billet of AM material fabricated using the LENS™ process. The SPPARKS generated synthetic microstructures used for upscaling have not been verified or validated against actual material microstructures – work on this is planned for FY 2020.

An important element of this work is the integration of upscaled representations of AM microstructures into analysis codes, such as ALEGRA, for the purpose of running microstructure-aware simulations. This was accomplished by the creation of an exodus file with element material properties not associated with blocks but with grain ids. Elements with the same grain id are assigned properties from a user specified distribution; in ALEGRA this is accomplished using the *Random Field* specification. In this way, properties such as modulus, yield stress, and other material model specific parameters can be distributed across the mesh that respects grain morphologies and length scales inherent with AM materials. For example, yield stress can be specified using a UNIFORM distribution with a particular MEAN value and maximum difference, ε, away from mean.

For the purpose of discussing preliminary and work-in-progress simulation results, a schematic of the test and the corresponding position vs. time, or x-t, diagram is shown in Figure 5-2. Details of the Thor experiment simulated are described in Section 4.1.2. The ALEGRA simulation models the Thor electromagnetic loading using a calibrated pressure pulse shown on the left of Figure 5-2. On the right, the VISAR system measures sample interface velocity as a function of time; using ALEGRA Lagrangian tracer points, simulated surface velocities are directly compared with measured VISAR velocities. Shown in Figure 5-3 is simulation results and VISAR measurement data for surface velocity. This result uses the JC fracture model for the purpose of capturing spall response shown in data. This simulation result is a work in progress, but nonetheless, shows a spall response. The JC fracture model is not ideal for capturing spall response, since it is more intended for conditions that are not relevant during the Thor experiment. This led to the development of the SKM as discussed in Section 3.2. A spall response is evident in the simulation results and is also shown in the x-t diagram of Figure 5-2, where tensile pressure conditions are observed in the sample at about 1.5 μs.

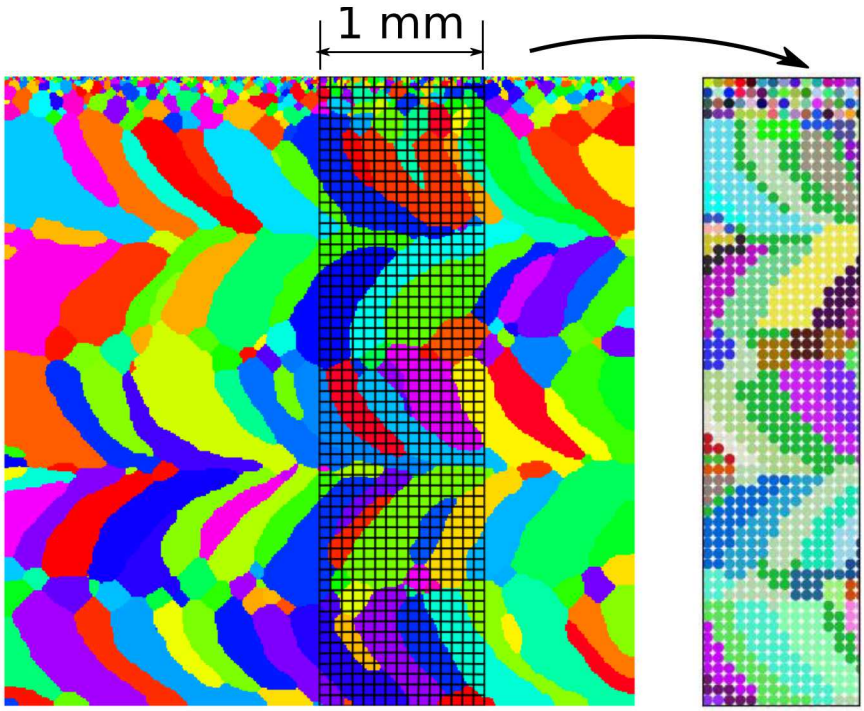

Figure 5-1. Overlay (left) and upscaled microstructure (right) used for test simulations.

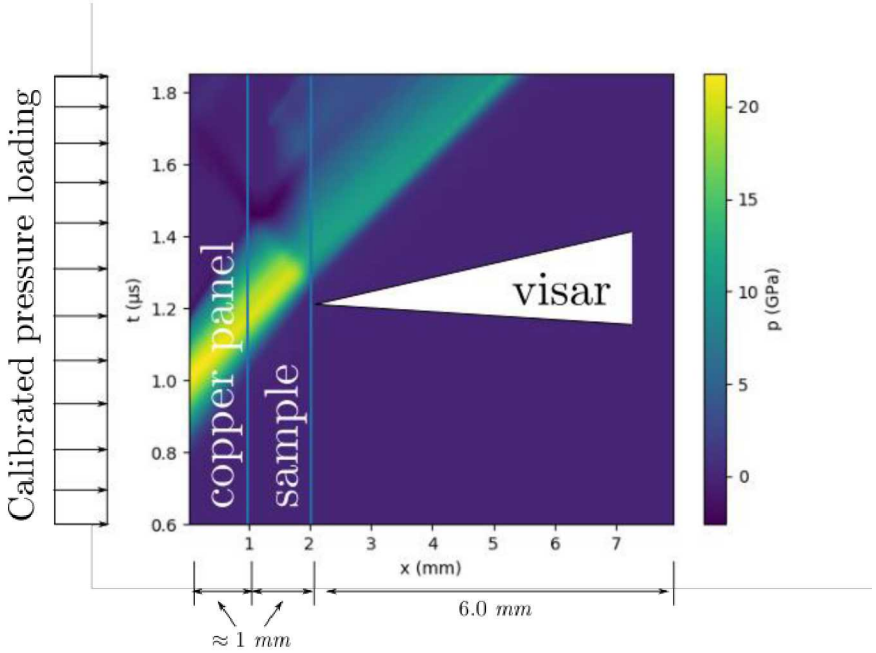

Figure 5-2. x-t diagram from ALEGRA simulation; uses JC fracture model for spall response. Tension and subsequent spall occur in the sample at ~ 1.45 μs.

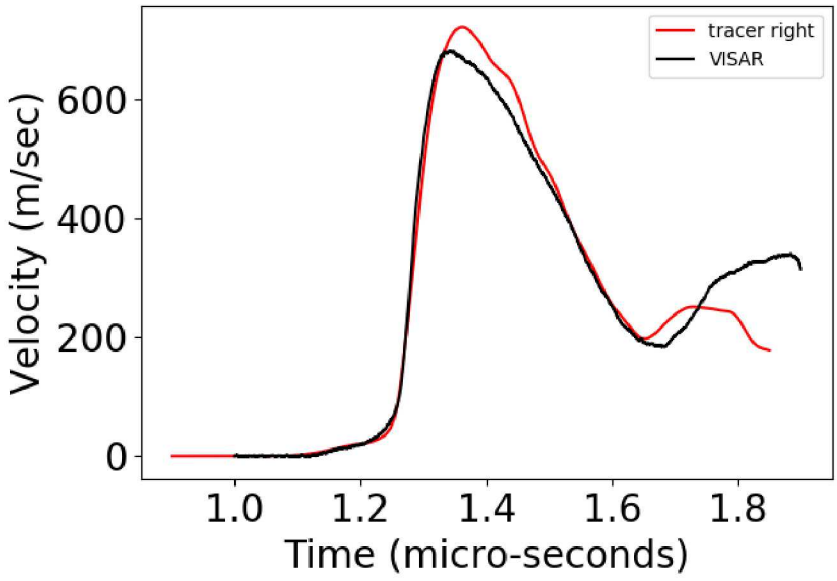

Figure 5-3. Comparison of the VISAR record from a ramp-release experiment on Thor to that obtained in ALEGRA using an upscaled representation of the AM microstructure.

5.2. Spall Kinetic Model

5.2.1. Plate Impact with VISAR data

A basic experiment for testing the spall response of materials uses plate impact with the impactor and plates designed to produce strongly tensile states of stress from internal wave reflections and superposition. Such an experiment is described in [24] and illustrated schematically in Figure 5-4.

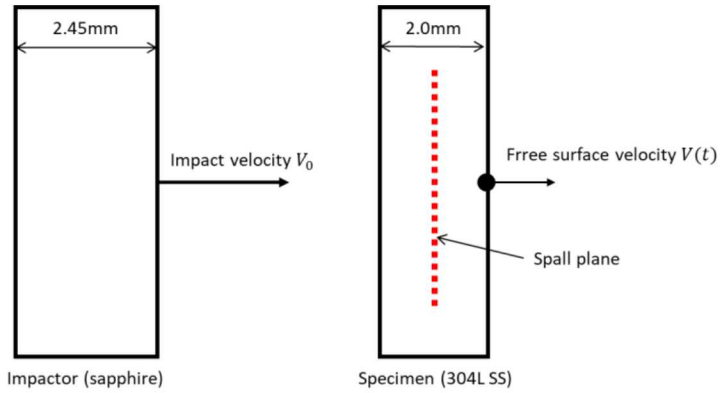

Figure 5-4. Plate impact experiment producing spall in the target specimen.

We modeled this experiment using a test version of CTH with the SKM implemented. Three different impact velocities were modeled: 154m/s, 247m/s, and 317m/s. These simulations were performed for both conventional wrought and AM 304L SS.

The SKM parameters were calibrated separately for the wrought and AM materials to achieve good agreement with free surface velocity data from prior experiments on identical wrought and AM 304L SS [24]. The resulting SKM parameters are summarized in Table 5-1. Equations for the SKM

showing how these parameters are used are described in [28]. The JC plasticity model and Mie-Gruneisen EOS were used for all materials with standard tabulated parameters.

Table 5-1. SKM parameters calibrated for wrought (W) and AM 304L SS along with wrought 316L SS.

Parameter	W 304L SS	AM 304L SS	W 316L SS	Units
Q_{stat}	-400	-400	-400	MPa
Q_∞	-2600	-3200	-2600	MPa
D	0.6	0.6	0.6	--
R	1.2	1.2	1.2	--
A	3500	3500	3500	MPa
B	1200	1200	1200	MPa
$\dot{\varepsilon}_\infty$	1.0E5	1.0E5	1.0E5	s^{-1}
$\dot{F}_0$	1.58E6	4.0E6	3.0E5	s^{-1}

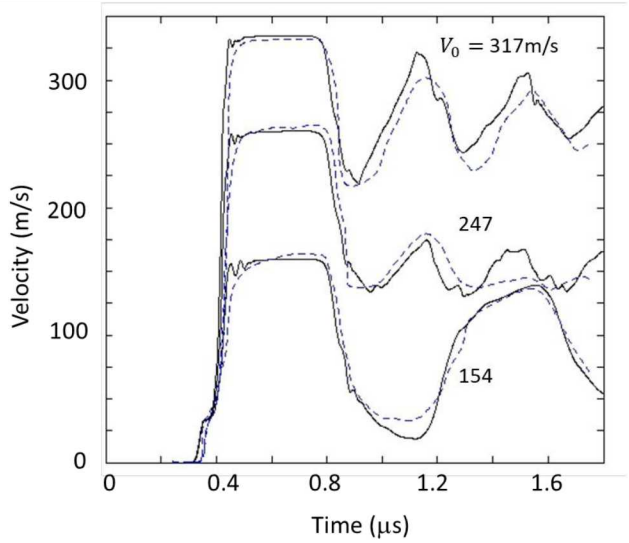

Figure 5-5. CTH model results with SKM compared with test data for free surface velocity in wrought 304L SS. Solid curves are model results. Dashed curves are experimental data [24].

The results for free surface velocity $V(t)$ are compared with test data from [24] in Figure 5-5 (for wrought) and Figure 5-6 (for AM). Solid black curves are the model results, and dashed blue lines are the test data from VISAR measurements. The agreement between the SKM simulations and the experimental data is quite good for both the wrought and AM 304L SS.

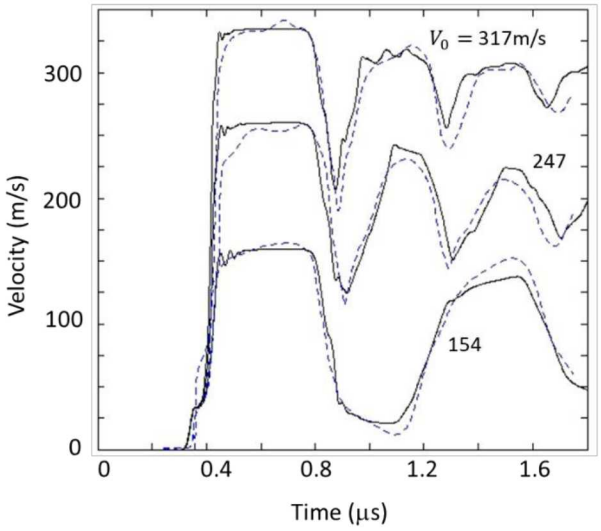

Figure 5-6. CTH model results with SKM compared with test data for free surface velocity in AM 304L SS. Solid curves are model results. Dashed curves are experimental data [24].

5.2.2. Plate Impact with Stress Gauge Data

As a further exercise of the SKM model as implemented in CTH, we simulated plate impact experiments with stress gauges [29]. In these experiments, a 2.5mm thick 316L stainless steel plate impacts a 5.0mm thick specimen made of the same material. A stress gauge is located in a polymethylmethacrylate (PMMA) block at the rear surface of the specimen.

The input parameters for 316L were taken to be the same as for 304L, except as shown in Table 5-1. The PMMA was modeled with the ANEOS [43] equation of state using standard tabulated parameters in the CTH material library. The CTH results are compared with test data from [29] in Figure 5-7. Once again, the agreement between the SKM simulations and the experimental data is quite good.

5.2.3. Triangular Shock Wave with Stress Gauge Data

Reference [29] also reports stress gauge data for a different configuration designed to produce a "triangular" (sharply peaked) wave propagating through the steel specimen. This wave is generated by using a heterogeneous impactor with a 1mm thick tungsten plate attached to a 5mm thick PMMA plate. The significance of the triangular wave profile for present purposes is that the spall surface is subjected to tensile loading over a shorter time interval than with the homogeneous steel impactor, which generates a flatter wave profile. Comparison of the SKM against experimental data is shown in Figure 5-8. The SKM simulations are seen to capture the general features of the experimental data, despite the model not being calibrated for such a loading condition. It suggests that the SKM formulation is accurately representing the spallation process.

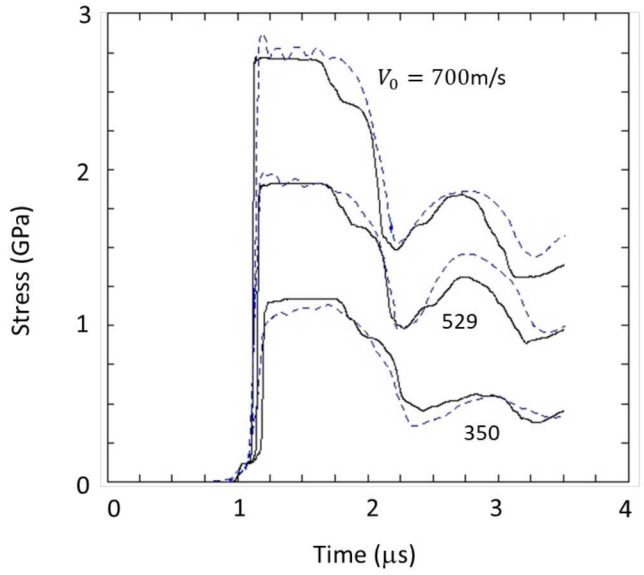

Figure 5-7. CTH model results with SKM compared with test data for stress at the rear surface of 316L SS. Solid curves are model results. Dashed curves are experimental data [28].

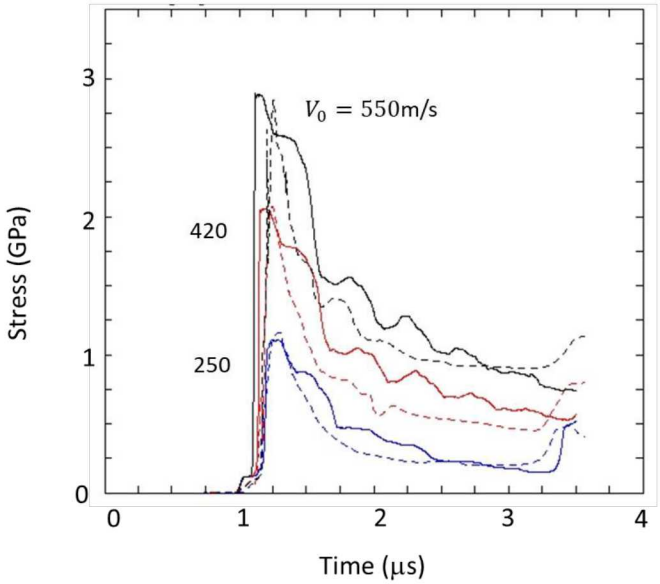

Figure 5-8. CTH model results with SKM compared with test data for stress at the rear surface of 316L SS impacted by a composite PMMA/tungsten projectile plate. Solid curves are model results. Dashed curves are experimental data [29].

6. PLANNED NEXT STEPS

The work and results presented in this report represent the current status of an ongoing project. Below are the planned areas of emphasis for the coming years.

6.1. Computational

Validation of SPPARKS generated microstructures is planned. This will require development to compare generated microstructures with material microstructures measured and observed using EBSD and/or traditional micrographs. Studies and use of the upscaled representations for AM microstructures in ALEGRA are planned; this capability was developed in FY 2019 but not explored; parametric and curve fitting studies are essential to demonstrate benefit and impact of this new capability. The SKM, described in Section 5.2, was implemented in ALEGRA at the end of FY 2019, but at the time of this writing was not at a stage to present results here; plans are to further develop this model as necessary to better capture the spall response.

To support validation, the following efforts are planned.

- Develop and demonstrate methods for validating SPPARKS microstructures for a given AM process.
- Using upscaled representations of AM microstructures, conduct ALEGRA simulations to understand microstructural effects on dynamic response; evaluate use of *random field* distribution parameters for spatially distributing properties on upscaled microstructures.
- Incorporate recently implemented SKM into simulations; improve fit to data shown in Figure 5-3. Determine how the use of upscaled microstructures affects the spall response.
- Using ALEGRA and upscaled microstructure representations of AM materials, study and evaluate use of upscaled microstructures for multipoint experimental measurements (described in Section 4.1.2.1.2). By looking at more than one point, a broader and more complete picture of the dynamic response of AM materials will be assessed. This is an effort to understand the effects of spatial material heterogeneities and length scales on dynamic response of AM materials.

6.2. Experimental

Finalizing the analysis of the all the dynamic experiments performed is ongoing and planned to be completed early in FY 2020. In addition, the following experimental investigations are planned for future years.

- One Z experiment was performed on heat treated AM microstructures (Table 4-1). Those heat treatments were chosen based on *in-situ* neutron diffraction studies that identified the annealing out of dislocations and ferrite, respectively [44]. Three Z experiments are planned to further investigate how those microstructural features influence flow strength at Mbar pressures.
- Thor experiments on single crystal austenitic stainless steel (FeCr18Ni12.5) are planned. Prior studies have identified large anisotropy in the elastic constants of single crystal stainless steels [45]. It is expected that large anisotropy will be observed between primary crystallographic orientations (i.e. [100] [010], and [001]) at dynamic strain rates.

Understanding the distribution in flow strength for various crystal orientations will help in defining the parameter distributions for our upscaled simulations.

- Study the spallation strength of AM material with prescribed voids. Collaborators at PSU are currently developing a method to put prescribed voids into an AM billet. These voids, of known shape and size, can then be placed at prescribed locations in a sample, enabling more controlled understanding of the influence of voids on the spall strength.
- Experiments using phase contrast imaging (PCI) at the Dynamic Compression Sector located at the Advanced Photon Source on Argonne National Laboratory [46] are planned to image the closure of a hole in wrought and AM material. Preliminary simulations using our microstructure upscaling technique predict the AM 304L SS will produce an asymmetric closure. Using PCI, images of the transient deformation can be obtained and compared to the simulations, provide a robust validation data set.
- Shock-release experiments are planned with thicker Al buffers to complete that experimental series.
- A Richtmyer-Meshkov instability (RMI) [47] platform has been under development on Thor. RMI experiments on wrought and AM 304L SS will provide another measurement of material strength.

REFERENCES

[1] L. E. Murr, S. M. Gaytan, D. A. Ramierez, E. Martinez, J. Hernandez, K. N. Amato, P. W. Shindo, F. R. Media and R. B. Wicker, "Metal fabrication by additive manufacturing using laser and electron beam metling technologies," *J. Mater. Sci. Technol.,* vol. 28, p. 1, 2012.

[2] W. J. Sames, F. A. List, S. Pannala, R. R. DeHoff and S. S. Babu, "The metallurgy and processing science of metal additive manufacturing," *Int. Matls. REv.,* vol. 61, p. 315, 2016.

[3] W. E. Frazier, "Metal additive manufacturing," *J. Matls. Eng. and Perf.,* vol. 23, p. 1917, 2014.

[4] Y. Zhai, D. A. Lado and J. Lagoy, "Additive manufacturing: Making imagination the major limitation," *J. Metals,* vol. 66, p. 808, 2014.

[5] A. N. Hopkinson and P. Dickens, "Analysis of rapid manufacturing - using layer manufacturing for production," *J. Mech. Eng. Sci.,* vol. 217, p. 31, 2003.

[6] T. J. Horn and O. A. Harrysson, "Overview of currrent additive manufacting technologies and selected applications," *Sci. Prog.,* vol. 95, p. 255, 2012.

[7] I. Gibson, D. W. Rosen and B. Stucker, Additive Manufacturing Technologies: Rapid Prototyping to Direct Manufacturing, New York: Springer, 2010.

[8] *Fiscal Year 2019 Stockpile Stewardship Managment Plan - Biennial Plan Summary,* U. S. Department of Energy, 2019.

[9] M. Griffith, M. Schlienger, L. D. Harwell, M. S. Oliver, M. Baldwin, M. E. M. T. Ensz, J. Brooks, C. V. Robino, J. E. Smugeresky, W. H. Hofmeister, M. J. Wert and D. V. Nelson, "Understanding thermal behavior in the LENS process," *Mat. Des.,* vol. 20, p. 107, 1999.

[10] P. Rangaswamy, T. M. Holden, R. B. Rogge and M. L. Griffith, "Residual stresses in components formed by the laser engineered net shaping (LENS) process," *J. Strain Anal. Eng.,* vol. 38, p. 519, 2003.

[11] D. P. Adams, B. Reedlunn, M. C. Maquire, B. Song, J. Carroll, J. E. Bishop, J. L. Wise, A. Kilgo, T. A. Palmer, D. W. Brown and B. Clausen, "Mechanical response of additively manufactured stainless steel 304L across a wide range of loading conditions," Sandia National Laboratories, SAND2019-7001, 2019.

[12] "Standard terminology for additive manufacturing - coordinate systems and test methodologies," ASTM International, West Conshohocken, PA, ISO/ASTM52921-13, 2013.

[13] J. L. Brown, C. S. Alexander, J. R. Asay, T. J. Vogler, D. H. Dolan and J. L. Belof, "Flow strength of tantalum under ramp compression to 250 GPa," *J. Appl. Phys.,* vol. 115, p. 043530, 2014.

[14] J. A. Mitchell, "An approach to upscaling SPPARKS generated synthetic microstructures of additively manufactured metals," Sandia National Laboratories, SAND2019-10873, 2019.

[15] S. Plimpton, A. Thompson and A. Slepoy, *SPPARKS,* htp://spparks.sandia.gov, 2016.

[16] S. Plimpton, C. Battaile, M. Chandross, L. Holm, V. Tikare, G. Wagner, E. Webb and X. Zhou, "Crossing the mesoscale no-man's land via parallel kinetic Monte Carlo," Sandia National Laboratories, SAND2009-6626, 2009.

[17] A. C. Robinson, T. A. Brunner, S. Carroll, R. Drake, C. J. Garasi, T. Gardiner, T. A. Haill, H. Hanshaw, D. Hensinger, D. LaBreche, R. Lemke, E. Love, C. Luchini, S. Mosso, J. Niederhaus, C. C. Ober, S. Petney, W. J. Rider, G. Scovassi, O. E. Strack, R. Summers, T.

Trucano, V. G. Wiers, M. Wong and T. Voth, in *46th AIAA Aerospace Sciences Meting and Exhibit*, 2008.

[18] T. M. Rodgers, J. D. Madison and V. Tikare, "Simulations of metal additive manufacturing microstructures using kinetic Monte Carlo," *Comp. Mater. Sci.,* vol. 135, p. 78, 2017.

[19] T. Rodgers, J. A. Mitchell and V. Tikare, "A Monte Carlo model for 3D grain evolution during welding," *Model simul. Mater. Sc.,* vol. 25, no. 6, p. 1, 2017.

[20] L. A. Schoof and V. R. Yarberry, "EXODUS II: A finite element data model," Sandia National Laboratories, SAND92-2137, 1992.

[21] E. Gruneisen, "Relation between compressibility, thermal expansion, atom volume and atomic heat of metals," *Annalen der Physik,* vol. 26, p. 394, 1908.

[22] *CTH v12.0,* Sandia National Laboratories, 2017.

[23] G. Johnson and W. Cook, "Fracture characteristics of three metals subjected to various strain, strain rates, temperatures and pressures," *Eng. Fract. Mech.,* vol. 21, no. 1, p. 31, 1985.

[24] J. L. Wise, D. P. Adams, E. E. Nishida, B. Song, M. C. Maquire, J. Carroll, B. Reedlunn, J. E. Bishop and T. A. Palmer, "Comparative shock response of additively manufactured versus conventionally wrought 304L stainless steel," *AIP Conf. Procc.,* vol. 1793, p. 100015, 2017.

[25] L. M. Barker and R. E. Hollenbach, "Laser interferometer for measuring high velocities of any reflecting surface," *J. Appl. Phys.,* vol. 43, p. 4669, 1972.

[26] G. R. Johnson and T. Holmquist, "Test data and computational strength and fracture model constants for 23 materials subjected to large strains, high strain rates and high temperatures," Los Alamos National Laboratory, LA-11463-MS, 198.

[27] G. Johnson and W. Cook, "A constitutive model and data for metals subjected to large strains, high strain rates and high temperatures," in *Proceedings of the Seventh International Symposium on Ballistics*, The Hague, The Netherlands, 1983.

[28] S. A. Silling, "Spall kinetics model description," Sandia National Laboratories, SAND2019-10345, 2019.

[29] G. T. Gray, N. K. Bourne and B. L. Henrie, "On the influence of loading profile upon the tensile failure of stainless steel," *J. Appl. Phys.,* vol. 101, no. 9, p. 093507, 2007.

[30] J.-P. Davis, J. L. Brown, M. Knudson and R. W. Lemke, "Analysis of shockless dynamic compression data on solids to multi-megabar pressures: Application to tantalum," *J. Appl. Phys.,* vol. 116, p. 204903, 2014.

[31] J. L. Brown, C. S. Alexander, J. R. Asay, T. J. Vogler and J. L. Ding, "Extracting strength from high pressure ramp-release experiments," *J. Appl. Phys.,* vol. 114, p. 223518, 2013.

[32] M. E. Savage, L. F. Bennett, D. E. Bliss, W. T. Clark, R. S. Coats, J. M. Elizondo, K. R. LeChein, H. C. Harkes, J. M. Lehr, J. E. Maenchen, D. H. McDaniel, M. F. Pasik, T. D. Pointon, A. C. Owen, D. B. Seidel, D. L. Smith, B. S. Stoltzfus, K. W. Struve, W. A. Stygar, L. K. Warne, J. R. Woodworth, C. W. Mendel, K. R. Prestwich, R. W. Shoup, D. L. Johnson, J. P. Corley, K. C. Hodge, T. C. Wagoner and P. E. Wakeland, "An overview of pulsed compression and power flow in the upgraded Z pulsed power dirver," in *IEEE Pulsed Power Conference*, Albuquerque, NM, 2007.

[33] M. E. Savage, K. R. LeChein, M. R. Lopez, B. S. Stoltzfus, W. A. Stygar, D. S. Artery, J. A. Lott and P. A. Corcoran, "Status of the Z pulsed power driver," in *IEEE Pulsed Power Conference*, Chicago, IL, 2011.

[34] D. B. Reisman, B. S. Stoltzfus, A. W. Stygar, K. N. Austin, E. M. Waisman, R. J. Hickman, J.-P. Davis, T. A. Haill, M. D. Knudson, C. T. Seagle, J. L. Brown, D. A. Goerz, R. B. Spielman, J. A. Goldlust and W. R. Cravey, "Pulsed power accelerator for materials physics experiments," *Phys. Rev. Accel. Beams,* vol. 98, p. 073530, 2015.

[35] R. W. Lemke, M. D. Knudson, D. E. Bliss, K. Cochrane, J.-P. Davis, A. A. Guinta, H. C. Harjes and S. A. Slutz, "Magnetically acclerated, ultrahigh velocity flyer plates for shock wave experiments," *J. Appl. Phys.,* vol. 98, p. 073530, 2005.

[36] R. W. Lemke, M. D. Knudson and J.-P. Davis, "Magnetically driven hyper-velocity launch capability at the Sandia Z accelerator," *Int. J. Impact Eng.,* vol. 38, p. 480, 2011.

[37] M. D. Knudson, "Megaamps, megagauss, and megabars: using the Sandia Z machine to perform extreme material dynamics experiments," *AIP Conf. Procc.,* vol. 1426, p. 35, 2011.

[38] S. P. Marsh, LASL Shock Hugoniot Data, Berkeley, CA: University of California Press, 1980.

[39] D. J. Steinberg, "Equation of state and strength properties of selected materials," Lawerence Livermore National Laboratory, UCRL-MA-106439, 1996.

[40] T. Arsenlis, N. R. Barton, C. Battaile, J. F. Benage, J. R. Brown, J. Brown, W. T. Buttler, S.-R. Chen, S. J. Fensin, D. G. Flicker, G. T. Gray, D. A. Jones, J. M. Lane, H. Lim, D. J. Lusher, R. Manzanares, D. T. Martinez, J. I. Martinez, T. Mattsson, H.-S. Park, M. B. Prime, D. W. Schmidt, K. L. Schmidt, S. K. Sjue, D. C. Swift and C. P. Trujillo, "Tri-lab tantalum strength milestone FY2018 Report," Sandia National Laboratories, SAND2018-10621, 2018.

[41] O. T. Strand, D. R. Goosman, C. Martinez, T. L. Whitworth and W. W. Kuhlow, "Compact system for high-speed velocimetry using heterodyne techniques," *Rev. Sci. Instrm.,* vol. 77, p. 083108, 2006.

[42] E. Daykin, M. Burk, D. Holtkamp, E. K. Miller, A. Rutkowshi, O. T. Strand, M. Pena, C. Perez and C. Gallegos, "Multiplexed photonic Doppler velocimetry for large channel count experiments," *AIP Conf. Proc.,* vol. 1793, p. 160004, 2015.

[43] S. L. Thompson, "ANEOS analytic equations of state for shock physics codes input manual," Sandia National Laboratories, SAND89-2951, 1989.

[44] D. W. Brown, D. P. Adams, L. Balogh, J. Carpenter, B. Clausen, G. King, B. Reedlunn, T. A. Palmer, M. C. Maguire and S. C. Vogel, "In situ neutron diffraction study of the influence of microstructure on the mechanical response of additively manufactured 304L stainless steel," *Metall. Mater. Trans. A,* vol. 48, no. 12, p. 6055, 2017.

[45] M. Kikuchi, "Elastic anisotropy and its temperature dependence of single crystals and polycrystals of 18-12 type stainless steel," *T. JPN. I. Met.,* vol. 12, p. 417, 1971.

[46] B. J. Jensen, S. N. Lua, D. E. Hooks, K. Fezzaa, K. J. Ramos, J. D. Yeager, K. Kwiatkoski, T. Shimada and D. M. Dattelbaum, "Ultrafast, high resolution, phase contrast imaging of impact response with synchrotron radiation," *AIP Advances,* vol. 2, p. 012170, 2012.

[47] M. B. Prime, W. T. Buttler, M. A. Buechler, N. A. Denissen, M. A. Kenamond, F. G. Mariam, J. I. Martinez, D. M. Oro, D. W. Schmidt, J. B. Stone, D. Tupa and W. Vogan-McNeil, "Estimation of metal strength at very high rates using free-surface Richtmyer-Meshkov instabilities," *J. Dynamic Behavior Mater.,* vol. 3, no. 2, p. 189, 2017.

DISTRIBUTION

Email—Internal

Name	Org.	Sandia Email Address
Dawn G. Flicker	1640	dgflick@sandia.gov
Christopher T. Seagle	1646	ctseagl@sandia.gov
David J. Littlewood	1444	djlittl@sandia.gov
Deidre Hirschfeld	1832	dhirsch@sandia.gov
Veena Tikare	1864	vtikare@sandia.gov
John A. Mitchell	1444	jamitch@sandia.gov
Stewart A. Silling	1444	sasilli@sandia.gov
Justin Brown	1646	jlbrown@sandia.gov
Jack Wise	1646	jlwise@sandia.gov
Brittany Branch	1646	babranc@sandia.gov
Paul Specht	1646	pespech@sandia.gov
David P. Adams	1832	dpadams@sandia.gov
Michael P. Saavedra	1832	mpsaave@sandia.gov
Corbett C. Battaile	1864	ccbatta@sandia.gov
Technical Library	01177	libref@sandia.gov

Email—External [redacted]

Name	Company Email Address	Company Name

This page left blank

This page left blank

Sandia National Laboratories

Sandia National Laboratories is a multimission laboratory managed and operated by National Technology & Engineering Solutions of Sandia LLC, a wholly owned subsidiary of Honeywell International Inc. for the U.S. Department of Energy's National Nuclear Security Administration under contract DE-NA0003525.